Radiations in Association with Lightning Discharges

Satoru Yoshida

Department of Information and Communications Technology
Division of Electrical, Electronic and Information Engineering
Graduate School of Engineering, Osaka University, Japan

July 2008

Preface

This thesis presents studies on radiations in association with lightning discharges. The contents of the thesis are based on the results of our research during the Ph.D. course at the Division of Information and Communications Engineering, Graduate School of Engineering, Osaka University. Lightning discharges have several complex processes, so that they cause radiations in an ultra wide frequency band; from very low frequency (VLF) to ultra high frequency (UHF) as well as optical radiations. Furthermore, many researchers reported the energetic radiations associated with lightning. In this thesis the energetic radiation means the photon radiations with energy from several hundreds keV to several tens MeV. The individual radiation corresponds to each complex process of the lightning discharge. One useful approach to the lightning physics is to observe and analyze the radiations associated with lightning. In the thesis, We focus on the energetic, electromagnetic, and optical radiations associated with lightning. In other words, we conducted lightning observation campaigns for energetic (Chapter 2) and electromagnetic radiations (Chapter 3), and performed observation data analyses for optical radiations from lightning (Chapter 4) in order to acquire knowledge concerning the physics of the atmospheric electricity, including lightning discharges.

The thesis consists of five chapters that are organized as follows:

Chapter 1 is the introduction of the thesis. The basic lightning physics and several terminologies are described briefly. We clearly show the motivations and significance of the thesis as well.

The main objective of Chapter 2 is to study energetic radiations associated with lightning. The energetic radiation has been one of the major topics in the field of the lightning physics since a runaway breakdown theory was proposed. According to the runaway breakdown theory, high energy particles, such as secondary cosmic rays, create high energy electrons by interaction with air. The high electric field leads to the high energy electrons by the runaway process, with photons appearing as these high energy electrons decelerate. This theory is one of the possible triggers of lightning, in other words, it is believed that the runaway breakdown theory is one of the keys to answer a basic and interesting question: How does lightning trigger? In this chapter, a field campaign was conducted during the winter thunderstorm season in Hokuriku, Japan. We recorded high energy photon and electron bursts accompanied by upward negative lightning and upward positive lightning. These results suggest that the photon bursts are caused by not only negative leaders but also positive leaders and the photon radiation has high energy electron bursts as well. The results in the thesis support the runaway breakdown theory strongly.

The objective of Chapter 3 is to study the charge transfer mechanism of upward lightning and the microwave radiation associated with lightning. We conducted lightning observation campaign with the use of a microwave receiver and a VHF broadband digital interferometer (DITF) during winter thunderstorm season in Hokuriku, Japan. This observation was conducted along with the energetic radiation observation described in Chapter 2. We recorded an upward flash striking a lightning protection tower and the flash was accompanied by six ICC pulses. Among them two ICC pulses had negative leaders prior to the ICC pulses. These preceding negative leaders probably caused the current increases of the ICC pulses, which means that the negative leaders created the channels for the ICC pulses. We recorded apparent increases in the microwave power associated with the upward lightning as well. The microwave radiation sources seem to be the tip of the negative leaders and the lightning current.

In Chapter 4, statistical data analyses are examined using the Lightning Imaging Sensor (LIS) and the Precipitation Radar (PR) data aboard the Tropical Rainfall Measuring Mission (TRMM) launched in 1997. The LIS detects optical emissions and locates the lightning discharges from space. In this chapter we have two main subjects. One is a parameterization of lightning by an aspect of a convective cloud. Knowledge of global lightning activity has grabbed attention in order to estimate the global NO_x production since lightning discharges are known as one of the major sources of NO_x on our planet. The parameterization of lightning is a useful technique to estimate the global lightning activity. From the eight-year analysis, we show that the number of lightning flashes per second per convective cloud is proportional to the fifth power of the snow depth. The other is a study of the impacts of the El Niño Southern Oscillation (ENSO) events on lightning activity in the Western Pacific Ocean, including South East Asia. The ENSO is a collective term of an El Niño and an La Niña, originally defined as events in which sea surface temperature in the waters off Peru increases or decreases. The study of these impacts of the ENSO events on the other parameters is important since it leads us to understand the mechanism of climate changes involving the ENSO. We show the remarkable contrasts associated with lightning activity between the El Niño and the La Niña events in the Western Pacific Ocean and discuss the reason why the contrasts appear as well.

Finally, Chapter 5 draws the conclusions of the thesis by summarizing all the results.

Acknowledgement

First, I would like to express my sincere gratitude to my supervisor, Professor Zen-Ichiro Kawasaki of Graduate School of Engineering, Osaka University, for his encouragement, valuable discussions, and meaningful advices throughout my studies. His many constructive comments and kind advices have greatly improved this work.

I am much indebted to Professor Tetsuya Takine of Graduate School of Engineering, Osaka University, who have given me many insightful suggestions for the thesis as an official reviewer. I take pleasure in thanking Professors Kenichi Kitayama, Shozo Komaki, Noboru Babaguchi, Seiichi Sampei, Kyou Inoue, Takashi Washio, and Riichiro Mizoguchi of Graduate School of Engineering, Osaka University, for providing thoughtful comments on this work.

I am deeply grateful to Professor Kenji Yamamoto of Graduate School of Engineering, Osaka University for discussion about my research, especially observation technique.

I am very grateful to Associate Professor Tomoo Ushio of Graduate School of Engineering, Osaka University for helping me a lot to carry out this work.

I am very grateful to Dr. Tatsuo Torii of Tsuruga Head Office, Japan Atomic Energy Agency, Tsuruga, Japan for a lot of useful discussions and helping me to carry out field observation campaign in Hokuriku. Without him, the studies concerning the energetic radiation associated with lightning would have not been developed well.

I also take pleasure in thanking Dr. Takeshi Morimoto, who is a lecturer of Graduate School of Engineering, Osaka University, for helping me a lot to carry out this work.

I would like to express my sincere appreciation to Professors Teiji Watanabe, Nobuyuki Takagi, and Associate Professor Wang Daohong of Graduate School of Engineering, Gifu University for their help with the field observation campaign in Hokuriku.

I thank Associate Professor Yushi Miura of Graduate School of Engineering, Osaka University, for help with the experiments.

In addition, I would like to thank Earle Williams in Massachusetts Institute of Technology for useful discussions and English corrections. I thank Peter Karagiannis of Graduate School of Frontier Biosciences and Mr. Etsuro Yoshii of the Okay Project School of English for English correcsions.

I am so much obliged to say thank you to all members of Kawasaki laboratory for their continuous encouragement and meaningful discussions. Special thanks go to Dr. Redy Mardiana, Messrs. Masatoki Kondo, Yosuke Sato, Shinji Oita, Masahito Sato, and Naotaka Nakazato.

Finally, I heartily thank my family, especially my wife Yuko, my sons Shintaro, and

Tomoya for their immense devotion, patience, and kindly support during the whole period of my life. They have always been giving me a lot of encouragement, which enabled me to accomplish the thesis.

Contents

Chapter 1

Introduction

1.1 Physics of lightning

A lightning discharge is one of the most well known natural phenomena and it is a sequence of neutralization between positive and negative charges, which are stored in the thundercloud. The lightning discharges are classified roughly into two types: one is a cloud-to-ground (CG) flash which bridges between thunderclouds and the ground, and the other is a cloud-to-cloud (CC) flash which occurs in a thundercloud or inter-thunderclouds. The CG flashes are sub-classified into four types according to their electrical polarity and the direction of the first leader, that is, downward negative lightning, downward positive lightning, upward negative lightning, and upward positive lightning. All four types and a CC flash are illustrated in Figure 1.1. It is widely known that the downward negative lightning (type (a)) accounts for more than 90% of CG flashes on our planet [1].

CG flashes basically consist of several processes: preliminary breakdowns, leader developments, return strokes, continuing currents, M-components, and so on. In the case of a downward negative flash, first, a negative stepped leader is launched toward the ground from negative charge region in the thundercloud. The stepped leaders sometimes involve a train of breakdown, called a preliminary breakdown. These trains of the preliminary breakdowns are defined as the in-cloud process that leads to the initiation of the downward moving negative stepped leaders [2]. The stepped leaders literally step in the air, in other words, repeat to stop and propagate while creating the conducting channel in the virgin air. The average propagation speed is of the order of 10^5 m/s [2]. Therefore, if it begins to develop at the attitude of 10 km in the thundercloud, it travels about 100 ms. After the contact of the downward stepped leader to the ground, an upward lightning current, called a return stroke, propagates toward the negative charge regions in the thundercloud at speed of the order of 10^8 m/s [2]. This sequence of the downward leader and the upward return stroke is termed a stroke. The return strokes are the most luminous event in the lightning, so what we see by our own eyes is the return strokes. Some CG flashes, called multiple lightning strokes, have two or more strokes, which consist of dart (dart-stepped) leaders and subsequent return strokes. After the stokes, relatively-small current,

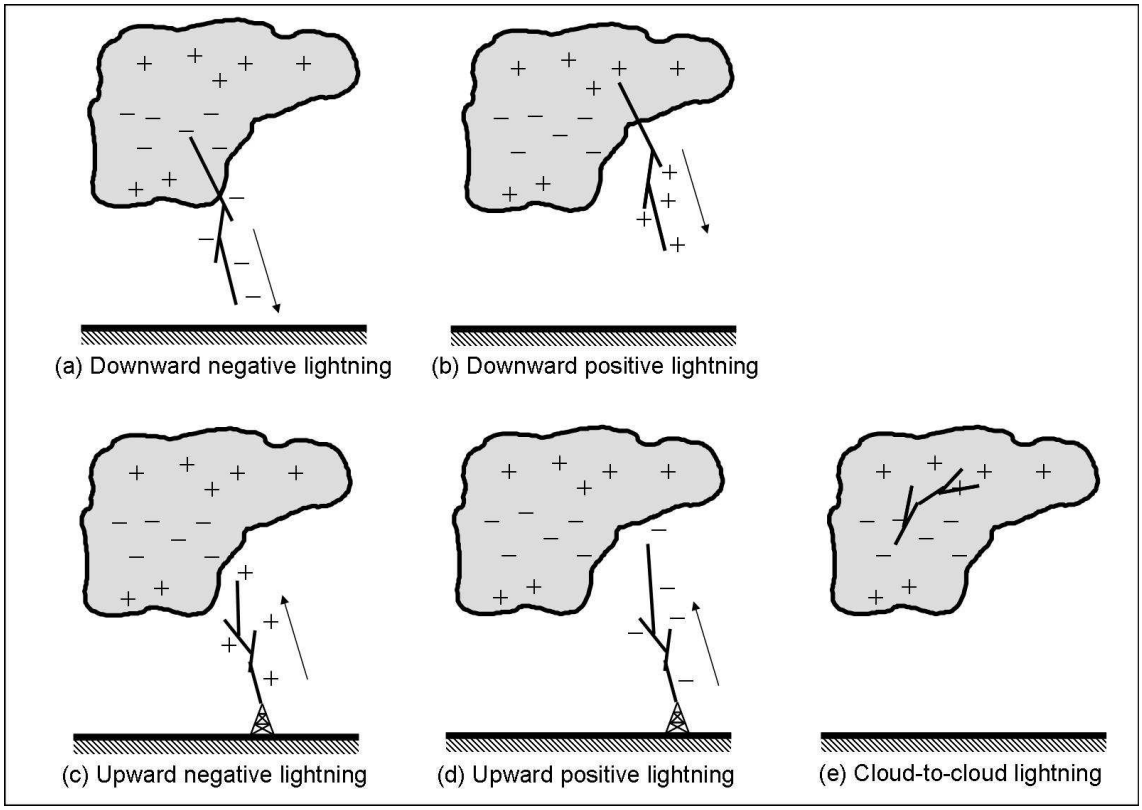

Figure 1.1: Illustrations of four type CG flashes and a CC flash. The CG flashes are classified according to their electrical polarity and the direction of the first leader. Only the initial leader is shown for each type.

which is termed a continuing current, flows between the thunderclouds and the ground. During a continuing current period, sometimes M-components occur. M-components are relatively higher currents than the continuing current and make the lightning channel luminous. In addition, during the time interval between return strokes, some CG flashes have J-processes and K-changes. The J-process and the K-change are defined as slow and fast changes, respectively, in E-field on the ground. Figure 1.2 indicates the schematic representation of the various processes comprising the negative CG flash.

In the case of upward lightning, an upward leader is initiated from a tall grounded-structure, such as a wind turbine and a tall tower, and develops toward the charge region in the thunderclouds [3]. That is why it is called "upward lightning". The upward lightning also has sequences similar to the downward lightning, namely, dart leaders, return strokes, continuing currents and M-components. One noticeable feature of the upward lightning is that more than 50% of upward flashes contain no stroke [3] and have only the initial stage (IS). The IS is the duration of rather long-term continuing current followed by the first upward leader development. The long-term continuing current is termed an initial continuing current (ICC), which sometimes lasts a few hundreds ms after the upward

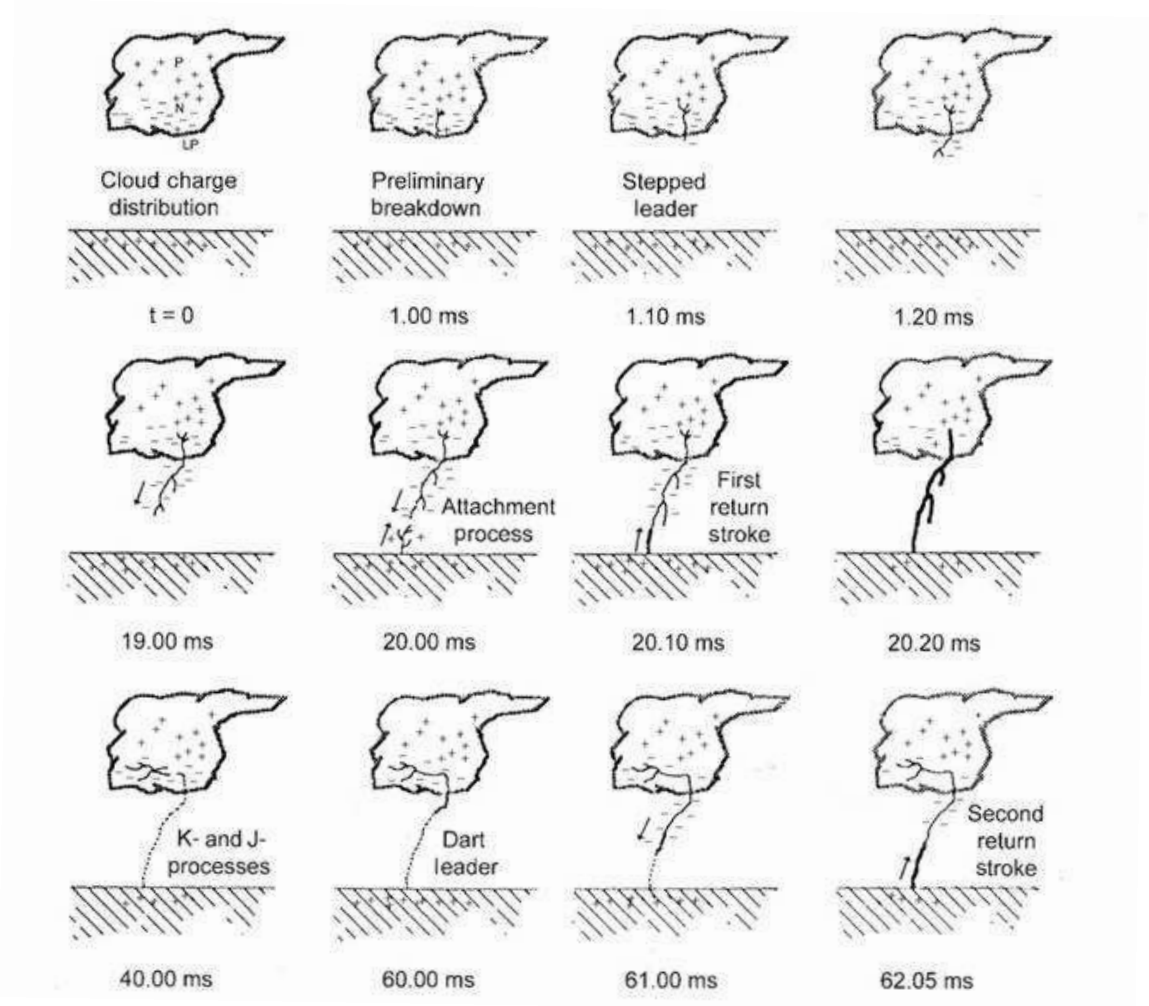

Figure 1.2: Various processes comprising a negative CG flash. Adopted from *Rakov and Uman* [2].

leader. Some ICCs involve ICC pulses, which are luminous events in the IS, and which are defined as abrupt lightning current changes.

CC flashes consist of an early (or active stage) and a late (or final) stage [4]. The early stage typically involves a negatively charged channel extending at an average speed of the order of 10^5 m/s. These processes in the early stage of the CC flash seem to correspond to the preliminary breakdowns and stepped leaders of CG flashes. In the late stage of the CC flash, negative charges are apparently transported to the region of the flash origin from remote sources in the negative charge region. The charge transfer process in CC flashes is termed a recoil streamer. The recoil streamers are accompanied by fast change in the E-field on the ground, so that they cause high current between the negative and positive charge region as in return strokes of the CG flashes.

In this way, the lightning discharges have several individual processes and complexly

intertwined with other processes.

1.2 Radiations in association with lightning

As we have described in the preceding section, the lightning discharges have several complex processes. All these processes are basically caused by movement of electrons. The bulk of movement of electrons causes a wide variety of radiations. Table 1.1 indicates the main radiations associated with lightning.

Electromagnetic waves in frequency bands from extremely low frequency (ELF) to low frequency (LF) are radiated from return strokes since return strokes transfer a great deal of electric charge over a long distance [5]. Some lightning locating systems (e.g., World Wide Lightning Location Network (WWLLN) [6] and Lightning Positioning And Tracking System (LPATS) [7]) detect electromagnetic waves in these low frequency bands and locate the points of the return strokes in two dimensions.

Electromagnetic waves in frequency bands from very high frequency (VHF) to ultra high frequency (UHF) are accompanied by leader developments, such as stepped leaders and dart leaders. These processes are the phenomena that the electric charges around the tip of the leaders travel as far as several tens meters. The VHF digital interferometer (DITF) has been developed in Lightning Research Group, Osaka University (LRG-OU) and is a system to locate sources of VHF impulses based on the digital interferometry [8, 9]. This system enables us to visualize the negative leader developments in 3 dimensions. One of the noticeable results of this system is to imply the charge distributions in the thunderclouds [10]. Lightning mapping systems, using these frequency bands, have achieved a great success and contributed to the development of lightning physics.

Optical emissions, including infra-red radiation and visible light, are mainly radiated from return strokes of the CG flash and recoil streamers of the CC flash. In the case of the return stroke, the peak current is of the order of 10 kA and the channel of the return strokes are heated up to 30,000 k [11]. The high temperature, even very short duration, causes optical radiations by thermal emissions and electron transitions ionized by the lightning current. The Lightning Imaging sensor (LIS) on the Tropical Rainfall Measuring Mission (TRMM) detects the optical emissions (wavelength $\lambda = 777.4nm$) and locates the lightning discharges from space [12]. Stepped leaders and dart stepped leaders also have optical emissions although the intensity of the optical signal is much less than those from the return strokes. An Automatic Lightning Progressing Feature Observation System (ALPS) is to detect weak optical emissions associated with leader developments [13].

Energetic radiation associated with lightning activity has been reported (e.g., [14]). In this thesis energetic radiation means photon radiations with energy from several hundreds keV to several tens MeV. These observation results are classified into two types according to the timing of the photon bursts. One is that the radiation bursts occur several ten seconds prior to CG flashes [15, 16]. In [15] and [16], these authors assert that such high energy photons are generated in the high electric field strength in the thunderclouds, and

Table 1.1: Radiations associated with lightning discharges.

Frequency bands	Lightning process	Radiation process
ELF $\sim$ LF	Return strokes	Charge transfer
VHF $\sim$ UHF	Leader developments	Electric current
IR	Return strokes Recoil streamers	Thermal emissions
Visible light	Leader developments M-components, ICC pulses	Electron transitions
X ray	Leader developments Charge separation	Runaway breakdown

these high energy photon bursts may initiate lightning flashes. One possible initiation of the runaway breakdown is an extensive atmospheric shower (EAS) that consists of a large number of different elementary particles and fragments of nuclei [17]. In this scenario, energetic secondary cosmic rays with energy of several MeV incident on the high E-field region in the thundercloud work as a "seed" of the runaway breakdown. After that, the runaway breakdown avalanche triggers the lightning discharge while increasing the number of free electrons.

On the other hand, many authors reported that radiation bursts on the ground are recoded coincidentally with negative leader development [18–22]. In this case, the energetic radiation bursts are inferred to be caused by the high electric field region around negative leaders [23]. Regardless of the two scenarios, it is widely believed that the high electric field leads to high energy electrons by the runaway process, with the photons appearing as these high energy electrons decelerate [23–25].

Lightning discharges involve a wide variety of radiations in the ultra wide band from ELF to X ray. These radiations are closely related to each lightning process which is intricately-intertwined with each other.

1.3 Objective and overview of this thesis

Lightning discharges cause radiations in the ultra wide frequency band. The each radiation corresponds to the processes of the lightning discharges. One useful approach to the lightning physics is to observe and analyze the radiations associated with lightning. Actually, the remote sensing has been playing an important role and giving a great deal of fruitful results in the field of lightning physics. Our research team (LRG-OU) has been studying the lightning discharges based on the remote sensing. We have worked as one of the members of the team. We have conducted field lightning observation campaign in Hokuriku, Japan, during winter thunderstorm seasons in 2006 - 2008. In addition, we have analyzed the LIS data on the TRMM. This thesis consists of five chapters, and

contents of each chapter are summarizes as follows;

In Chapter 2, we focus on the mechanism of the runaway breakdown. The runaway breakdown process is one of the possible triggers of lightning [17]. Many observation results (e.g., [14]), reporting energetic radiations associated with lightning activity, inferred that the radiation sources are the E-field strength in the thundercloud and/or the tip of the negative leaders. In this regard there are two interesting questions. One is the existence of the electron bursts associated with lightning, being predicted from the runaway breakdown theory. To show the existence of the electron bursts as well as photon bursts associated with lightning is evidence to support the existence of the runaway breakdown process in association with lightning. The other is the exisitence of energetic radiation bursts associated with positive leaders of natural lightning. No one has reported energetic radiation bursts associated with the positive leaders of natural lightning. Now the runaway breakdown theory has been developed based on the hypotheses that the runaway breakdown should occur in the thundercloud [26] and/or the tip of the negative leaders [22]. The evidence of energetic radiations associated with the positive leaders will change the view of the mechanism of the runaway breakdown.

A field campaign was conducted during the winter thunderstorm season in Hokuriku using a NaI scintillator and a thin plastic scintillator (PS), which primarily detects high energy electrons. The winter thunderstorm season in Hokuriku has remarkable features. One is that the charge regions in the thunderclouds are located at a lower altitude than in other regions [27]. This feature is suited to detect the energetic radiations from lightning since the energetic radiation travels only as far as a few kilometers. We recorded high energy photon and electron bursts accompanied by upward negative lightning and upward positive lightning. These results suggest that photon bursts are caused by not only negative leaders but also positive leaders and the photon radiations have high energy electron bursts as well. This study proofed the occurrence of the runaway breakdown associated with lightning discharges and gave a new question concerning the mechanism of the runaway breakdown process associated with positive leaders.

In Chapter 3, there are two objectives. The first objective is to clarify the charge transfer mechanisms of the ICC pulses of the upward lightning. The upward lightning has long-term ICC, causing great charge transfer [28] and a lot of damage to the triggered structures like a wind turbine [29]. The understanding of the mechanism, especially how the charges in the thunderclouds are transferred, of the ICC is needed in the fields of engineering as well as science. To clarify the ICC pulses, a lightning observation campaign was conducted with a use of the VHF broadband DITF, a capacitive antenna, and a microwave receiver during winter thunderstorm season in Japan. The VHF broadband DITF visualizes the negative leader developments, which means that it enables us to know how the charges are transferred in the thunderclouds. In the campaign, an upward flash striking a lightning protection tower was recognized and the upward flash had six ICC pulses. Among them two ICC pulses, which have fast risetimes, were accompanied by negative leaders prior to the ICC pulses. The current increases of the ICC pulses seem to be caused by these negative leaders, which means that the negative leaders produced the channels for the ICC pulses. The observation results indicate that the mechanism of the ICC pulses

are similar to the stepped leader - return stroke sequence.

The second objective in Chapter 3 is to examine when and how microwave radiations associated with lightning occur. We have been designing and manufacturing the lightning localization system by means of microwave radiations. The microwaves have much shorter wavelengths than the wavelengths of the electromagnetic waves which are now used for the lightning mappers. A "microwave lightning location system" can be a more accurate lightning mapper than the other lightning localization systems based on the electromagnetic wave observations. As the first step of this study, the microwave power associated with lightning was measured. We recorded apparent increases in the microwave power associated with the upward lightning. The observation results imply that the microwave radiation sources are the tip of the negative leaders and the lightning current and a possibility of a new lightning system by means of microwave emissions.

In Chapter 4, the results of two statistical data analyses are examined, using the LIS and the Precipitation Radar (PR) data aboard the TRMM. Contrast to the ground-based observations, the satellite observation allows us to acquire the useful data not only on the land but also on the ocean. The long-term and bulky data provided by the TRMM observation are well suited to conduct statistical analysis. One analysis is a parameterization of lightning by an aspect of a convective cloud (Section 4.3). From the eight-year analysis, we show that the number of lightning flashes per second per convective cloud is proportional to the fifth power of the snow depth. This parameterization enables us to obtain knowledge of global lightning activity in order to estimate the global NO_x production. The other is a study of the impacts of the El Niño Southern Oscillation (ENSO) events on lightning activity in the Western Pacific Ocean (Section 4.4). We show the remarkable contrasts associated with lightning activity between the El Niño and the La Niña in the Western Pacific Ocean and discuss the reason why the contrasts appear as well.

In Chapter 5, all results shown in the former chapters are summarized.

Chapter 2

Energetic radiations from lightning

2.1 Introduction

A field campaign was conducted during the Japanese winter thunderstorm season to observe radiation bursts associated with lightning discharges using a NaI scintillator and a thin plastic scintillator (PS), which primarily detects high energy electrons. This chapter presents the observation results and discussions. In Section 2.2, the background of this study is described in details. In Sections 2.3 and 2.4, the observation method and the observation results are shown. Finally, in Section 2.5, the discussions of the observation results and summary of the chapter are shown.

2.2 Background

The relationship between radiation bursts and lightning activity has been extensively studied since *Wilson* [30] suggested the possibility of bremsstrahlung radiation in the high electric field region of a thundercloud. Recently, many radiation bursts in association with lightning discharges have been reported. *Moore et al.* [31] reported that radiation bursts with energies in excess of 1 MeV lasted several milliseconds before the first return strokes of the negative cloud-to-ground (CG) flashes. *Dwyer et al.* [18, 19, 21] also reported that radiation bursts with energies up to a few hundred keV were associated with the stepped-leaders, dart leaders, and return strokes. Furthermore, several radiation bursts measured on satellites have also been reported [32, 33].

These studies suggest the possibility that the high electric field leads to high energy electrons by the runaway process, with the photons appearing as these high energy electrons decelerate [17, 23–25]. Such energetic radiation bursts have been recently observed on the ground and from space, and are inferred to be caused by the high electric field region around negative leaders, which involve a lot of negative breakdowns [22].

In this study, we have observed high energy electron bursts and photon bursts from both negative and positive lightning discharges.

2.3 Observation

A field observation campaign for lightning discharges in Hokuriku, Japan, which borders the Sea of Japan, was conducted from November 2006 to February 2007. Two radiation detectors and a capacitive E-field antenna were installed at a site about 400 m away from a wind turbine and its lightning protection tower. At the foot of this wind-generator apparatus, two Rogowski coils were equipped to measure lightning currents. Furthermore, a VHF broadband digital interferometer (DITF) was installed about 8 km away from the wind turbine. All systems were synchronized with GPS.

The first radiation detector consisted of one rectangular parallel-piped plastic scintillator (PS) covered by a foil of 24-μm-thick aluminum on the upper side and two photomultiplier tube (PMT) detectors attached to the bottom side (see Figure 2.1). The PS had a length of 800 mm, a width of 300 mm, and a thickness of 0.2 mm. This detector was entirely covered with a 0.05-mm-thick black plastic bag. The amplifier (AMP) filtered the thermal noise from the PMT signal and converted the signal into a 700 ns TTL pulse. The PS was so thin compared to the photon range that most photons passed through the PS without interacting with it. The high energy electron range, however, was short enough to interact with the PS (see Figure 2.2). Thus the PS primarily recorded high energy electrons. The PS was tested in the laboratory using radioactive sources. Figure 2.3 shows the PS detection efficiency for beta rays and gamma rays, respectively, defined by the ratio of the number of particles detected by the PS to the number of particles incident on the

Figure 2.1: A photo of the PS.

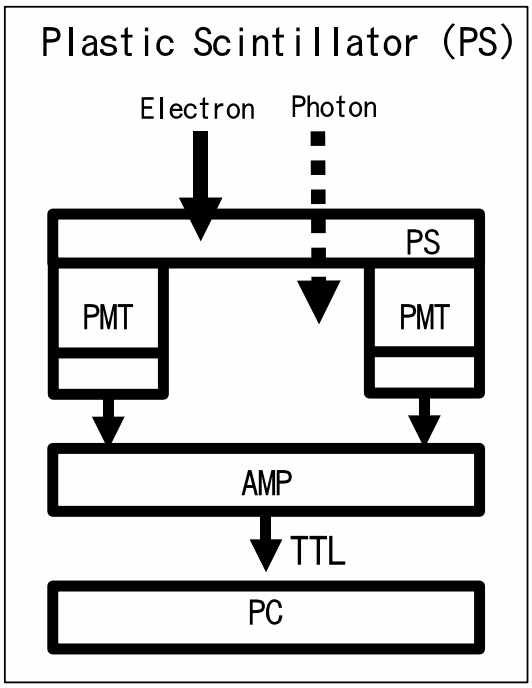

Figure 2.2: A schematic diagram of the PS.

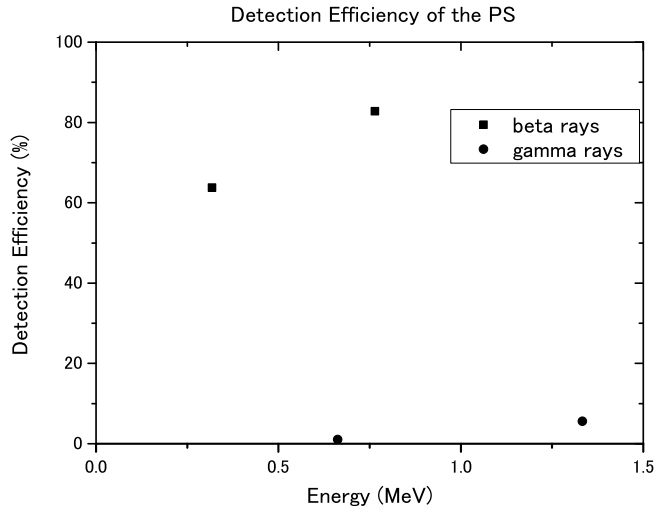

Figure 2.3: The PS detection efficiency for beta and gamma radiation in the laboratory using radioactive sources (^{60}Co and ^{204}Tl for beta rays; ^{137}Cs and ^{60}Co for gamma rays). The dots in the panel correspond to the actual measurement values. The energy value for each dot corresponds to the endpoint energy of each beta ray source. A dot of gamma rays at 1.33 MeV includes the effect of 1.17MeV since we employ ^{60}Co.

PS from the radioactive sources (^{60}Co and ^{204}Tl for beta rays; ^{137}Cs and ^{60}Co for gamma rays). A simple Monte Carlo simulation indicated that the PS could detect beta rays with energies from 100 keV to 10 MeV and that the detection efficiency for 100 keV gamma rays was below 0.02%. The measurement and simulation results indicate that the PS detected beta rays with energies in excess of approximately 100 keV, and that the response ratio for the beta rays was almost twenty times higher than that of gamma rays. In order to check the response of the equipment, we performed a series of tests including placing the PS under a bright flashlight and direct sunlight. We also set the PS at a distance of 8.7 m from a surge generator which produced high voltage sparks and emitted strong electromagnetic waves in various frequency bands. In all these experiments the background rate in the PS count rate did not show any considerable increase. The PS was mounted on a board at a height of 50 cm above the ground. The downside of the PS was shielded from ground environmental radiation by 2 rectangle boards made of copper with 20 mm thickness on the upper side and lead with 50 mm thickness on the lower side.

The other radiation detector consisted of one 7.6 cm diameter by 7.6 cm thick cylinder of a NaI(Tl) scintillation detector mounted on a PMT (see Figure 2.4). This detector was entirely covered with a 1-mm-thick aluminum cylinder. Each signal from the NaI was converted to a 600 ns TTL pulse using an AMP. Since this detector was a cylindrical scintillation detector, both high energy photons and electrons were recorded. The dis-

Figure 2.4: A photo of the NaI.

crimination energy level was set at 430 keV, in other words, the NaI detects radiations with energies in excess of 430 keV. Multiple lower energy radiations arriving in a fast burst, however, could produce one count. This detector was housed in a wooden box and mounted on the roof of the hut at a height of 2.6 m. The TTL pulses from both the PS and the NaI were measured using the same counter (Contec; CNT32-4MT) at 1 ms sampling interval, that is, the counter records the number of TTL pulses at intervals of 1 ms. The background count rates of the PS and the NaI detectors were less than 0.2 counts/ms.

The capacitive E-field antenna has a time constant of 2.2 sec. Its output was recorded at a sampling interval of 0.1 μs. The Rogowski coil system at the wind turbine could measure lightning currents as high as 12.6 kA at sampling interval of 2 μs. Since the Rogowski coil installed to the tower measured the electric current through only one foot of the tower, which has four feet, the electric current through the whole tower is estimated as the quadrupled values of the measurement values. The VHF broadband DITF could locate wideband VHF impulsive electromagnetic radiation sources of lightning in two dimensions [8, 9].

2.4 Results

During the observation period, a total of 7 lightning flashes occurred on the wind turbine or the lightning protection tower. For these 7 events, the count rate of the NaI detector exhibited an apparent increase. The count rate of PS, however, exhibited an apparent increase in only 3 events. We report the results for only 2 interesting events, which are an upward positive lightning (Flash A) and an upward negative lightning (Flash B), respectively.

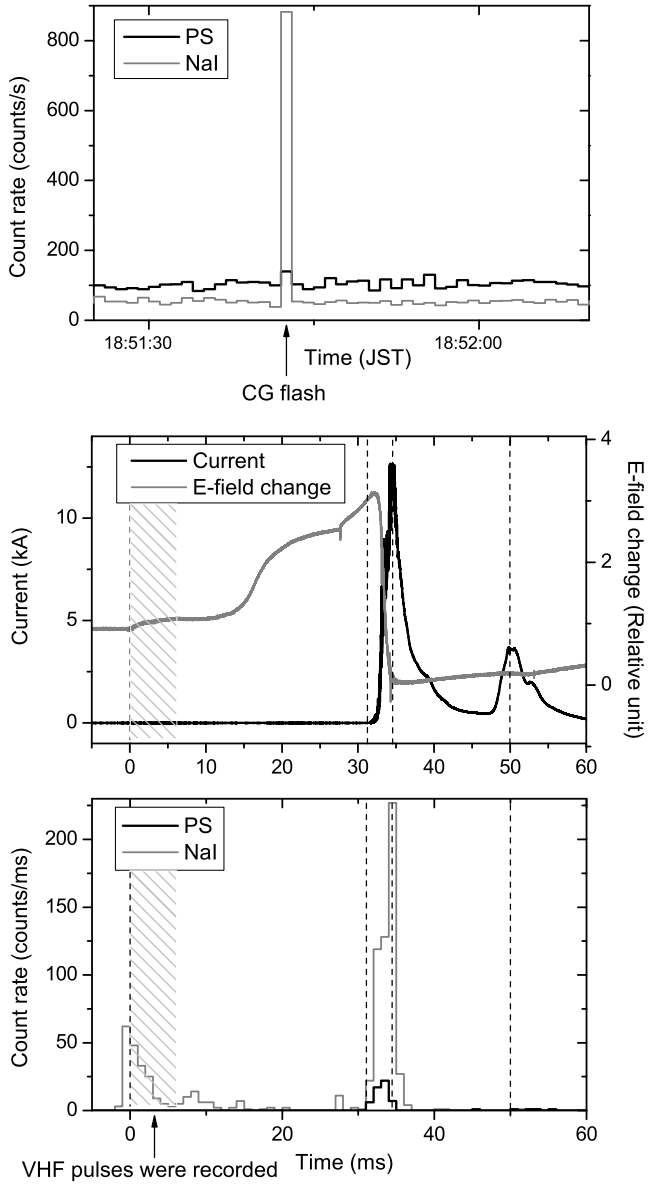

Figure 2.5: The count rates, the E-field change, and the lightning current of Flash A on the 6th of January in 2007. The lightning struck the wind turbine at 18:51:42 (JST). Count rates (counts/s) of the PS and the NaI (top panel), the E-field change on the ground, the lightning current measured at the foot of the wind turbine (middle panel), and the count rates (counts/ms) of the PS and the NaI detectors (bottom panel).

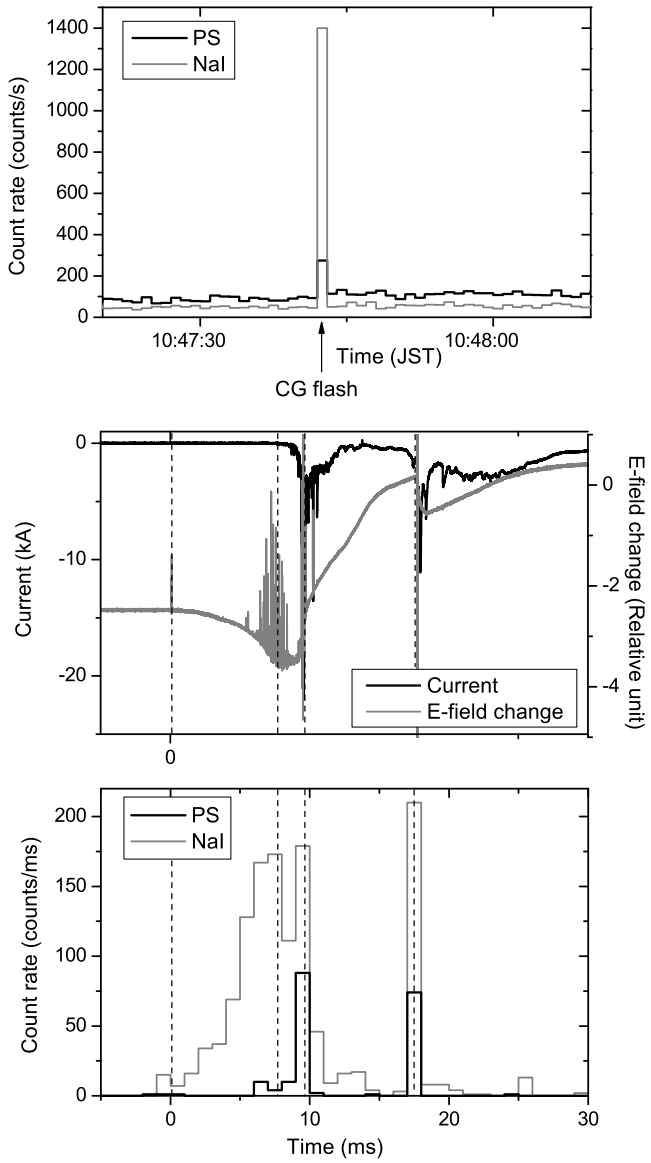

Figure 2.6: Similar to Figure 2.5 but for Flash B recorded at 10:47:42 (JST) on the 17th of December in 2006. The lightning struck the lightning protection tower. Count rates (counts/s) of the PS and the NaI (top panel), the E-field change on the ground, the lightning current measured at the foot of the lightning protection tower (middle panel), and the count rates (counts/ms) of the PS and the NaI detectors (bottom panel).

Flash A

This lightning flash struck the wind turbine at 18:51:42 (JST) on the 6th of January in 2007. The top panel of Figure 2.5 shows the count rates (counts/s) of the PS and the NaI

detectors during a period of 45 seconds around the lightning. As seen from this panel, the NaI and PS count rates increased only at the time when the flash struck, which is different from previous reports [15], where those authors reported radiation bursts more than several tens of seconds prior to a lightning flash. The middle and the bottom panels of Figure 2.5 show a detailed comparison between the count rates in counts/ms of the PS and the NaI detectors and the simultaneously recorded E-field and current waveforms. In this thesis, the E-field change waveforms are shown based on the atmospheric sign convention; a positive current value implies that a positive current flows from the cloud to the ground. As evident from the current waveform and the corresponding E-field waveform, the event was a positive CG flash initiated by an upward negative leader from the wind turbine at 34 ms, since the current waveform is similar to the typical one of the upward positive lightning [3]. Prior to the current increase, a positive E-field change was noticeable between 0 ms and 30 ms. This is likely caused by a nearby intracloud discharge that triggered an upward negative leader [29]. For this event, 2048 VHF pulses were recorded in the first 7 ms by the VHF broadband digital interferometer. These "noisy VHF radiations" are caused by negative leaders [34]. Taking account of the E-field change, we conclude that a negative breakdown should be involved in the intracloud discharge and would also move away from our capacitive E-field antenna. The lightning current was saturated at 34 ms with a magnitude of 12.6 kA. This current showed a second peak of 3.6 kA at 50 ms.

The first count rate burst on the NaI detector appeared from around the beginning of the E-field change. It returned to zero at 20 ms. Accompanied with the initiation of the upward negative leader, both PS and NaI count rates showed significant increases and then reached their peaks, 22 counts/ms for PS at 33 ms and 227 counts/ms for NaI at 34 ms. These peaks are roughly in correspondence with the electric current peak. After 40 ms there was no significant increase in either the PS or the NaI count rates.

Flash B

This lightning flash hit the tower at 10:47:42 (JST) on the 17th of December in 2006. The top panel of Figure 2.6 shows the count rates (counts/s) of the PS and the NaI detectors during a period of 50 seconds around the lightning. Similar to Flash A, the NaI and PS count rates increased only at the time when the flash struck. The middle and the bottom panels of Figure 2.6 are for a detailed comparison between the count rates in counts/ms of the PS and the NaI, and the simultaneously recorded E-field and current waveforms. As identified from the current and the corresponding E-field waveforms, the event was a negative CG flash initiated by an upward positive leader from the tower at 8 ms. Prior to the apparent increase in electric current, a negative E-field change was seen between 0 ms and 8 ms. Similar to Flash A, this electric field change is identified as being caused by a nearby intracloud discharge that triggered the upward positive leader [29]. Moreover, many pulses occurred in the E-field changes during this period, similar to previous reports [35, 36]. It is reasonable to assume that these pulses correspond to the developments of negative breakdowns. From the E-field change waveform, it seems that the negative breakdown was approaching the capacitive E-field antenna. The lightning current showed

a peak at 9.6 ms with a magnitude of 22 kA. After the upward positive leader, the lightning current remained negative and had several impulses between 10 ms and 15 ms.

The NaI count rate burst appeared from around the beginning of the E-field change. It increased until 9 ms. Accompanied with the initiation of the upward positive leader, both PS and NaI count rates showed significant increases and then reached their peaks; 88 counts/ms for the PS at 33 ms and 174 counts/ms for the NaI detector at 9 ms. These peaks are roughly in correspondence with the current peak.

2.5 Summary and Discussion

A field observation campaign was conducted during the winter thunderstorm season in order to study high energy electron and photon bursts associated with lightning discharges. Bursts of high energy electrons with energies in excess of 100 keV were recorded. The radiation detected by the NaI and the PS detectors is consistent with bremsstrahlung produced by energetic electrons associated with lightning. A Monte Carlo simulation showed that 10 MeV electrons can travel up to 50 m in air. This suggests that high energy electron ranges with energies up to several MeV are much shorter than the distance between lightning paths and the PS. Therefore the high energy electrons detected by the PS did not come directly from leaders in the thundercloud. We speculate that these high energy electrons were produced by high energy photon interactions such as Compton scattering near the PS. The high energy photons were generated by the leader of the thundercloud and traveled to the observation site.

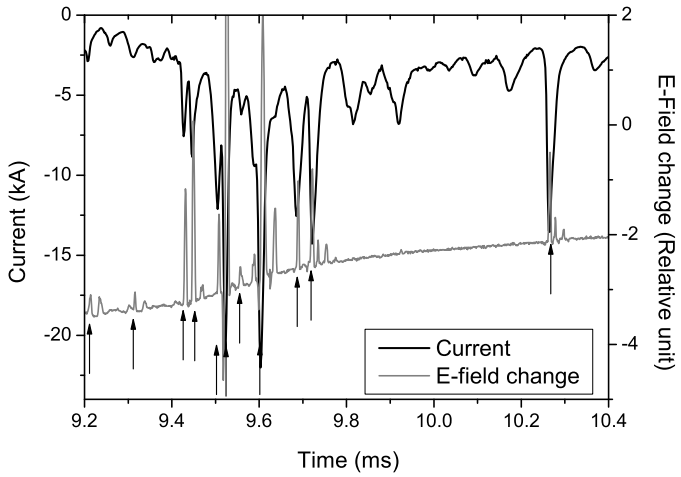

Figure 2.7: Expanded waveforms for comparing the E-field change pulse and current pulse for Flash B between 9.2 ms and 10.4 ms. The black arrows indicate the E-field pulses corresponding to the current pulses.

The increases in the NaI count rate prior to the upward leaders seems to be caused by the intracloud discharges that involved the negative breakdowns. These results are consistent with previous results [23]. Even though the radiation bursts associated with positive breakdowns in the laboratory have been reported by *Dwyer et al.* [37], this study is the first to present a piece of evidence that a positive leader of natural lightning could also cause the increase in the NaI count rate. As seen in Figure 2.6 for Flash B, after the upward positive leader started, several pulses appeared in both the electric field change and the current. An expanded waveform comparing the E-field change pulse and current pulse is shown in Figure 2.7. The black arrows indicate the E-field pulses corresponding to the current pulses. Except for a few E-field pulses that are smaller than the pulses appearing before the upward leader, the E-field pulses correspond apparently to the current pulses. These E-field pulses are identified as being caused by the upward leader. Upward leaders in Japanese winter lightning usually involve some pulses as reported by *Wang et al.* [38]. These pulses are likely to be related to the increase in the NaI count rate. A few small pulses in E-field change that do not correspond to the current pulses might be caused by negative discharges nearby. These negative discharges, however, did not have a significant impact on the NaI count rate.

Chapter 3

Electromagnetic radiations from lightning

3.1 Introduction

During winter thunderstorm season in Japan, a lightning observation campaign was conducted with a use of a microwave receiver and a VHF broadband digital interferometer (DITF). The main objects of this campaign is to understand the charge transfer mechanism of the ICC pulse and to examine when and how microwave radiations occur associated with lightning. In this chapter, the observation results and discussions are presented. In Section 3.2, the background of this study is described in details. In Sections 3.3 and 3.4, the observation method and the observation results are shown, respectvely. In Section 3.5, the possible mechanisms of the ICC pulses and the radiation sources of the microwave associated with lightning are discussed based on the observation results. Finally, in Section 3.6, all contents in this chapter are summarized.

3.2 Background

Characteristics of upward lightning have been investigated since *McEachron* [39] reported the existence of upward lightning on their observations of lightning currents and photographic images for the first time. The upward lighting begins with an upward leader, which is initiated from a high-grounded object and develops toward charge regions in the thunderclouds. After the upward leader, an initial continuing current (ICC) lasts in several hundred milliseconds [40]. Subsequent processes, such as return strokes and the following continuing currents, sometimes occur after an initial stage (IS), involving the upward leader and the ICC [41]. The IS often has multiple upward branches that develop toward charge regions in the thunderclouds independently [3]. It seems that this characteristic of the IS sometimes causes much greater charge transfer than the downward lightning [3] and serious damage to the triggered objects such as a wind turbine [29]. Therefore the understanding of the mechanism of the IS is needed in the fields of science as well as

engineering.

Recently, ICC pulses, which are luminous events in the IS, have been paid attention. This luminous event is similar to an M-component during the continuing current that follows a return stroke in both natural and triggered lightning [42, 43]. Many researchers measured some parameters concerning the ICC pulses and compared the characteristics of the ICC pulses with those of M-components.

Wang et al. [44] showed some lightning current parameters of the ICC pulses of the negative rocket-triggered lightning, such as the risetime, the half peak width, and the charge transfer. They concluded that all characteristics of the ICC pulses strongly resemble those of the M-components reported by *Thottappillil et al* [45]. From the observation of the upward lightning at Peissenberg tower in Germany, *Fuchs et al.* [41] reported a median peak current for the ICC pulse was 3.9 kA, which is considerably larger than the geometric mean (GM) value (312 A) of the current of the ICC pulses in the triggered lightning reported by *Wang et al.* [44].

Miki et al. [46] compared the observation results of the ICC pulses of upward lightning observed in several regions with triggered lightning in Florida. They showed that the ICC pulses of upward lightning tend to have larger current peaks and smaller durations, risetimes, and half peak widths than those of the triggered lightning. In addition, some ICC pulses of the upward lightning have a short risetime less than 1 μs in the lightning current. Since the risetime of these fast pulses is similar to the risetime of current pulses in association with return strokes, they presumed that these fast rise ICC pulses are cased by a sequence similar to the leader - return stroke. In other words, negative leaders are initiated from the space charge regions and connect to the channel of the ICC. These assumptions are supported by the optical observation results [28, 47]. Moreover, from the observations during winter thunderstorm season in Fukui, Japan, *Miki et al.* [48] reported the results that additional luminous channel connecting to the luminous current channel of the ICC appeared after the fast rise ICC pulse.

The results reported by *Miki et al.* [48] strongly support the hypothesis presented by *Miki et al.* [46]. Their results, however, have shown no leader development before the fast rise ICC pulse. In order to prove the hypothesis, we conducted lightning observation campaign during winter thunderstorm season in Japan. The first objective of this campaign is to present the observation results in association with negative leader developments prior to the fast rise ICC pulses.

The second objective of this campaign is to examine when and how microwaves are radiated from lightning discharges. Although many years have been passed since it was reported that electromagnetic radiations at microwave frequencies are accompanied by lightning discharges [49], only a few observations at these frequencies have been conducted [50]. So far, remote sensing systems for lightning discharge using electromagnetic waves up to several hundreds MHz have enabled us to understand the lightning physics (e.g., [10]). Since the wavelength of the microwave is much shorter than the electromagnetic waves at several hundreds MHz, the studies on the mechanisms of the microwave radiation associated with lightning lead us to establish a new lightning localization system that can map the lightning discharges more precisely than lightning localization system

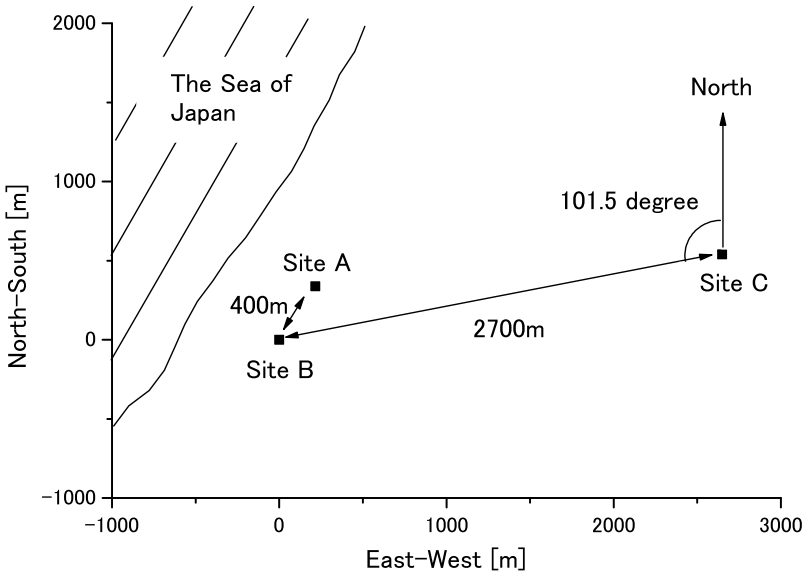

Figure 3.1: Sketch map of the observation sites.

detecting electromagnetic waves at lower frequency bands. In order to examine when and how the microwave radiations associated with lightning occur, the microwave measurements were also made in conjunction with the observations.

In this chapter, the observation results concerning the fast rise ICC pulses are shown as well as the microwave radiations associated with upward lightning.

3.3 Observation

A field observation campaign for lightning discharges in Uchinada-chou, Ishikawa prefecture of Japan, which borders the Sea of Japan, was conducted from December 2007 to January 2008. Figure 3.1 shows the sketch map of the observation sites. The microwave receiver was installed at Site A, while Rogowski coils on the feet of a 100 m high wind turbine and a 105 m high lightning protection tower were equipped at Site B to measure lightning current. A VHF broadband digital interferometer (DITF), a capacitive E-field antenna, and a video camera were installed at Site C. The distance between Sites A and B was 400 m, while the distance between Sites B and C was 2.7 km. The direction from Site C toward Site B made an angle of 101.5° to the north. The heights of Sites A and B were about 40 m above the sea level, while the height of Site C was very close to the sea level.

The microwave receiver consisted of a down-converter and a pyramidal horn antenna, designed for receiving effectively electromagnetic waves from 2.6 GHz to 3.95 GHz. The

maximum gain of the antenna was 15 dB, and a half-power beamwidth of the E-plane and H-plane were 30.6° and 31.0° at 2.9 GHz, respectively. The antenna was set up toward the lightning tower at 30° in elevation so that the antenna received mainly the microwave radiations from the approximately-square area between the tip of the lightning tower and the point 300 m above the tip. Each electrical signal at a frequency of 2.9 GHz from the antenna was down-converted to 500 kHz and digitalized in a PC with a 1 μs sampling interval.

The Rogowski coil system installed to the foot of the tower measured lightning currents as high as 13.5 kA at sampling interval of 2 μs in the frequency range between 0.5 Hz and 100 kHz. Since the Rogowski coil measured the electric current through only one foot of the tower, which has four feet, the electric current through the whole tower was estimated as the quadrupled values of the measurement values.

The VHF broadband DITF located impulses of wideband VHF electromagnetic radiation sources in two dimensions [8, 9]. The VHF broadband DITF consisted of capacitive antennas that were equipped at three apexes of a level isosceles right-angled triangle with a separation of 10 m. The received broadband signals from lightning were limited by a band-pass filter with the pass band of 20-100 MHz and digitalized by a digital oscilloscope at 4 ns sampling interval. The basic idea of the broadband digital interferometry is to estimate phase differences between the impulsive electromagnetic wave pulses received by a pair of two antennas. In this system, two independent phase differences were acquired. If an arrival direction meets the two incident angles, the direction of an electromagnetic source was estimated in terms of elevation and azimuth [9].

One of the remarkable features of the VHF broadband DITF is to have wide detection frequency range. Since the Fast Fourier Transform (FFT) was applied for data processing, we acquired as many phase differences as Fourier components in each pair of antenna for each VHF pulse. From the redundancy of the phase difference, the accurate estimation of the directions of VHF radiation sources were realized [9].

The capacitive E-field antenna measured E-field change on the ground. The capacitive antenna has a time constant of 10 s at sampling interval of 977 ns. The video camera was set up toward the lightning tower and enabled us to acquire optical images in a 33 frame/sec.

3.4 Results

During the observation period, four CG flashes struck on the lightning protection tower. All flashes are identified as upward negative lightning from the tip of the tower. For these four events, the waveform of the microwave power exhibited apparent increases, and lightning currents were recorded. The VHF broadband DITF as well as the capacitive antenna, however, recorded only one flash. In this study, the one flash that all detectors detected simultaneously is shown.

The lightning flash struck the lightning protection tower at 3:37:05 (JST) on the 31st of December in 2007 (Figure 3.2). In Figure 3.2, the first two panels show the two dimen-

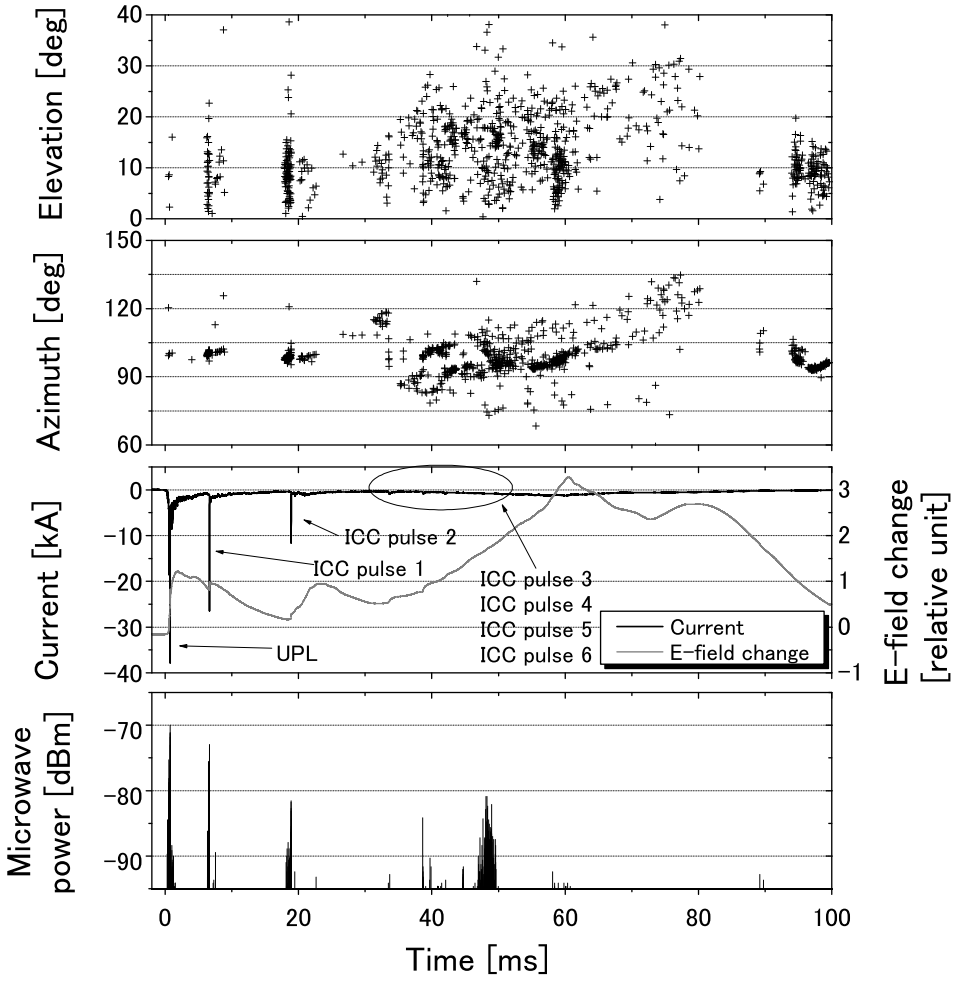

Figure 3.2: The two-dimensional mapping of the VHF electromagnetic waves from Site C (the first two panels), the lightning current and E-field change (the third panel), and the microwave power (the bottom panel) of upward lightning. The upward lightning struck the lightning protection tower at 3:37:05 (JST) on the 31st of December in 2007.

sional VHF impulse sources located by the VHF broadband DITF, elevation and azimuth from Site C , respectively. The third and bottom panels of Figure 3.2 show the lightning current waveform measured at the foot of the tower and E-field change at Site C, and received microwave power at Site A as a bar in each 1 μs, respectively. The time zero corresponds to the triggered time of the VHF broadband DITF. As in Chapter 2, E-field change waveforms are shown based on the atmospheric sign convention; a positive current value indicates that a positive current flows from the cloud to the ground. The lightning

Figure 3.3: One image of the video camera installed at Site C for the upward lightning. The left luminous channel is the upward lightning, while the other luminous channel is the lightning flash occurred nearby.

current waveform indicates the polarity of this lightning flash was negative. By high speed camera observation at Site A, this event was identified as a concurrent flash [51, 52] that several flashes occur simultaneously. In other words, an upward positive leader was launched from the tip of the tower prior to the lightning that was not striking the tower. The observation results of the high speed camera indicate that the following lightning began to develop about 45.2 ms. Therefore, at least after 45.2 ms, the observation data except lightning current are a mix of the two flashes. Figure 3.3 shows an optical image of the video camera installed at Site C. We recognize two luminous channels; the left one was hitting the tower and the other was not hitting the tower in Figure 3.3. In this study we focus on only the upward lightning launched from the tip of the tower.

After the first peak in the current waveform, the current value remained negative over whole the flash. The flash has only the IS and does not have any return strokes. In this event, seven abrupt changes in the lightning current are recognized. The first change in the lightning current is identified as an upward positive leader (UPL) followed by an ICC. We term the seven changes in the lightning current UPL, ICC pulse 1, 2, 3, 4, 5, and 6, respectivedly, from the left in Figure 3.2.

Figure 3.4 shows the extension of Figure 3.2 around the UPL. The error bars in the first two panels mean the standard deviations calculated from the law of propagation of errors for elevation and azimuth for each VHF electromagnetic pulse. As seen in the third panel of Figure 3.4 the waveform in the lightning current has a train of several impulses that are similar to the pulsations of upward leaders reported by several authors [46, 53]. *Miki et al.* [46] reported that these impulsive current waveforms in the IS were caused by the stepping process of upward leaders. Therefore, in this period, the UPL propagated

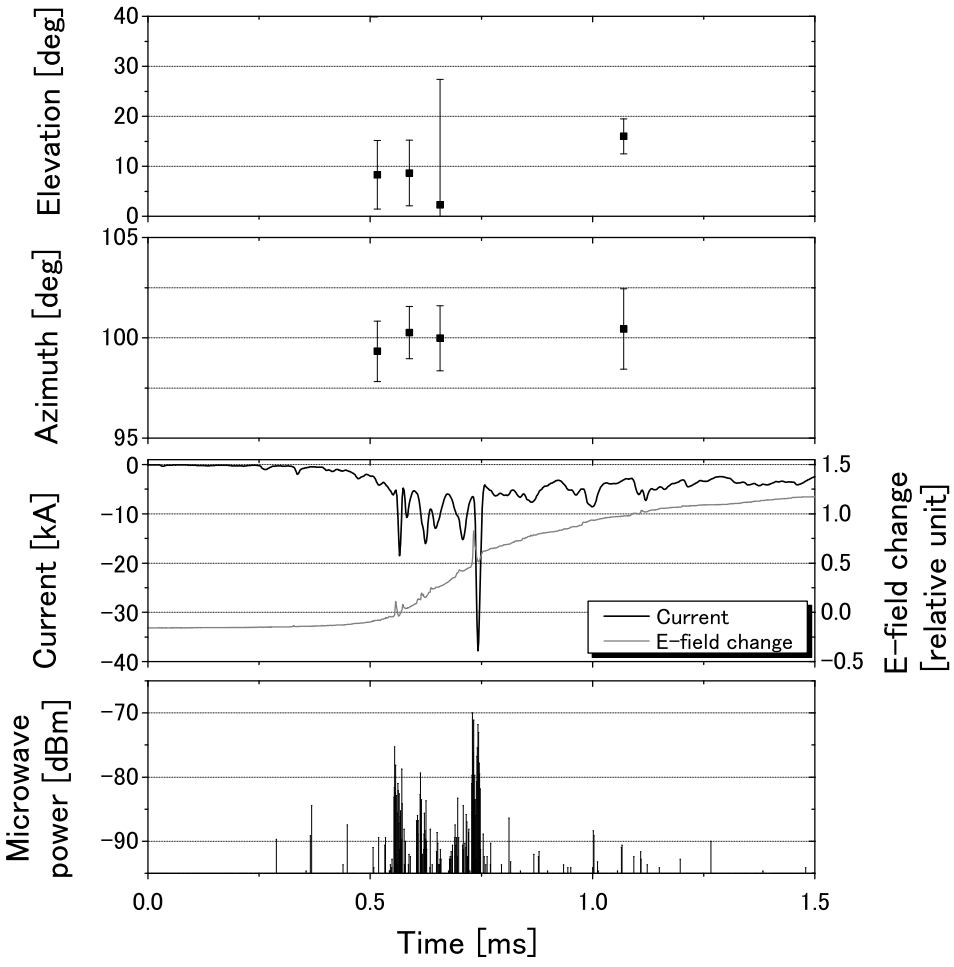

Figure 3.4: The extension of Figure 3.2 between 0 ms and 1.5 ms around the UPL. The error bars in the first top panels mean the standard deviations calculated from the law of propagation of errors for elevation and azimuth for each VHF electromagnetic pulse.

through virgin air until the arrival to the main charge region in the thundercloud. The impulsive waveform lasted about 30 ms after the beginning of the UPL. If the UPL propagated at a speed of 10^5 m/s on a typical average value reported by *Rakov* [54], the UPL traveled about 3 km or so. The main charges transferred to the ground by the UPL were probably located at the height of 2 or 3 km from the sea level.

As seen in the first two panels of Figure 3.4, a few VHF sources are mapped in association with the development of the UPL. Those VHF pulses were located around 100° in azimuth. Since the lightning protection tower was located in the direction of 101.5° in azimuth from Site C, these VHF pulses are likely to be radiated from the upward leader.

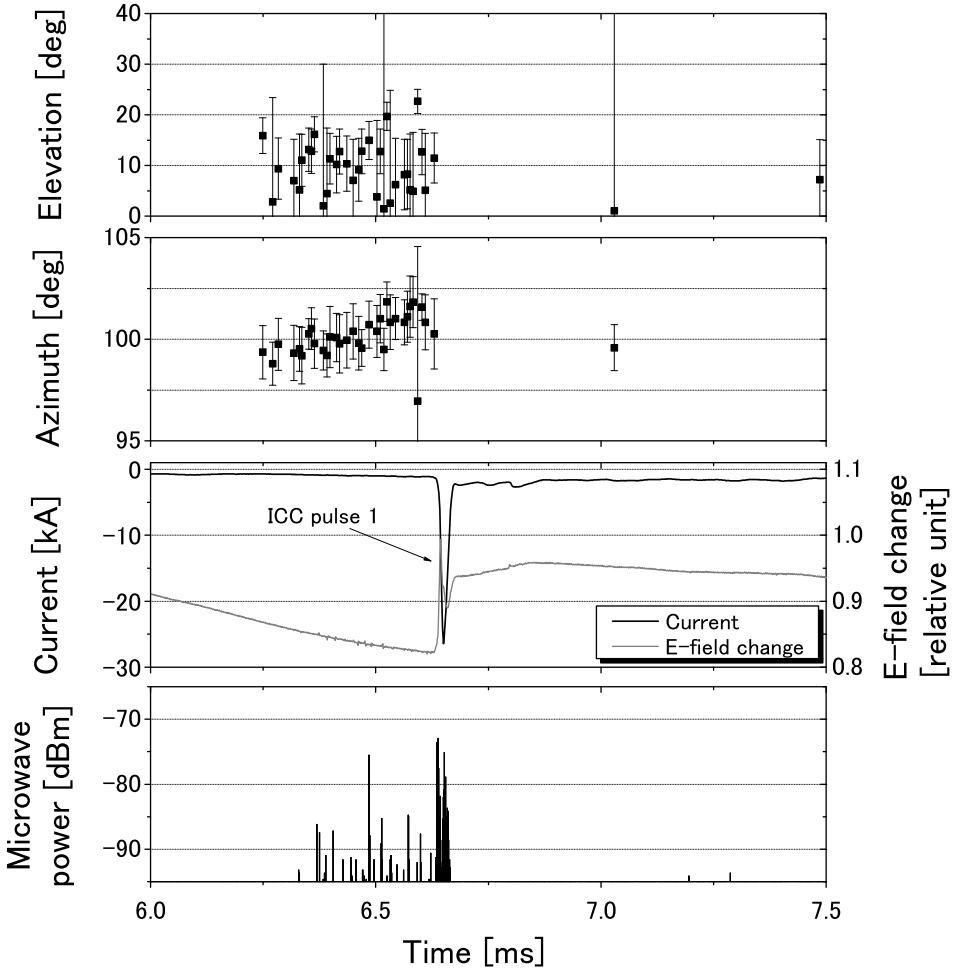

Figure 3.5: The extension of Figure 3.2 between 6 ms and 7.5 ms around the ICC pulse 1. In the third panel, the peak in the lightning current corresponds to the ICC pulse 1.

According to the previous reports (e.g., [34]), positive leaders cause less intense radiations than negative leaders do. Therefore only a few sources were located by the VHF broadband DITF. The elevation angles of the UPL shown in the top panel of Figure 3.4 do not go upward with time. The VHF location technique employed in this study could not map well the low elevation [8]. Although the leader really developed upward, the upward developments are not shown in the VHF mapping since the radiation sources were located in low elevations. The bottom panel of Figure 3.4 shows the increases in the microwave power accompanied by the development of the UPL.

The extension of Figure 3.2 around the ICC pulse 1 is shown in Figure 3.5. As see in Figure 3.5, many VHF impulses were recorded prior to the ICC pulse 1, while a few

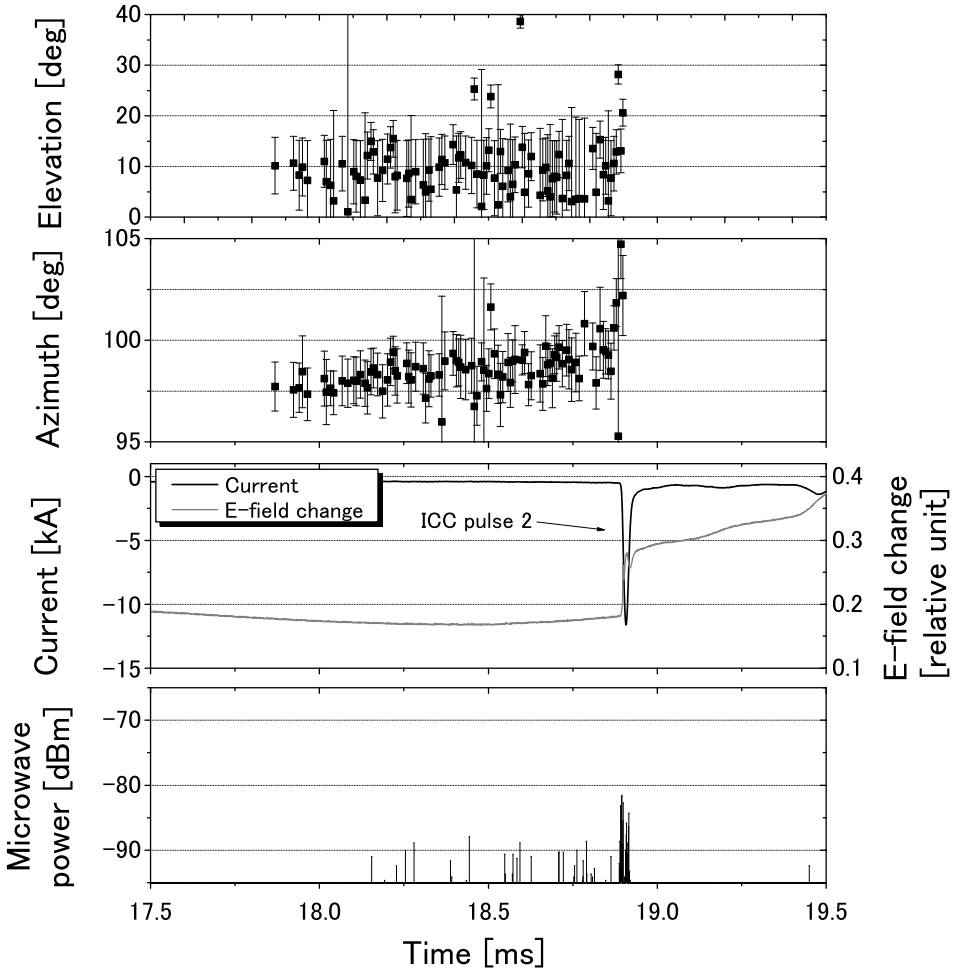

Figure 3.6: The extension of Figure 3.2 between 17.5 ms and 19.5 ms around ICC pulse 2. In the third panel, the peak in the lightning current corresponds to the ICC pulse 2.

VHF pulses were recorded after the ICC pulse 1. Since most of the sources located by the VHF mapper correspond to negative breakdowns (e.g., [34]), the train of VHF radiations is identified as a negative leader. The preceding negative leader developed from 99° to 102° in azimuth. Since no branch of this upward lightning is recognized in Figure 3.3, the preceding negative leader propagated within the thundercloud. The preceding negative leader is likely to be initiated near the tower and connect to the channel of the ICC in the thundercloud. The pulse peak of the lightning current, which is defined as the pulse peak in the lightning current from the ICC, is 26 kA. The charge transfer caused by the ICC pulse 1, which is defined as a time integral of the lightning current from the ICC, is 655 mC and the 10-90% risetime in the lightning current of the ICC pulse 1 is 8 μs. The

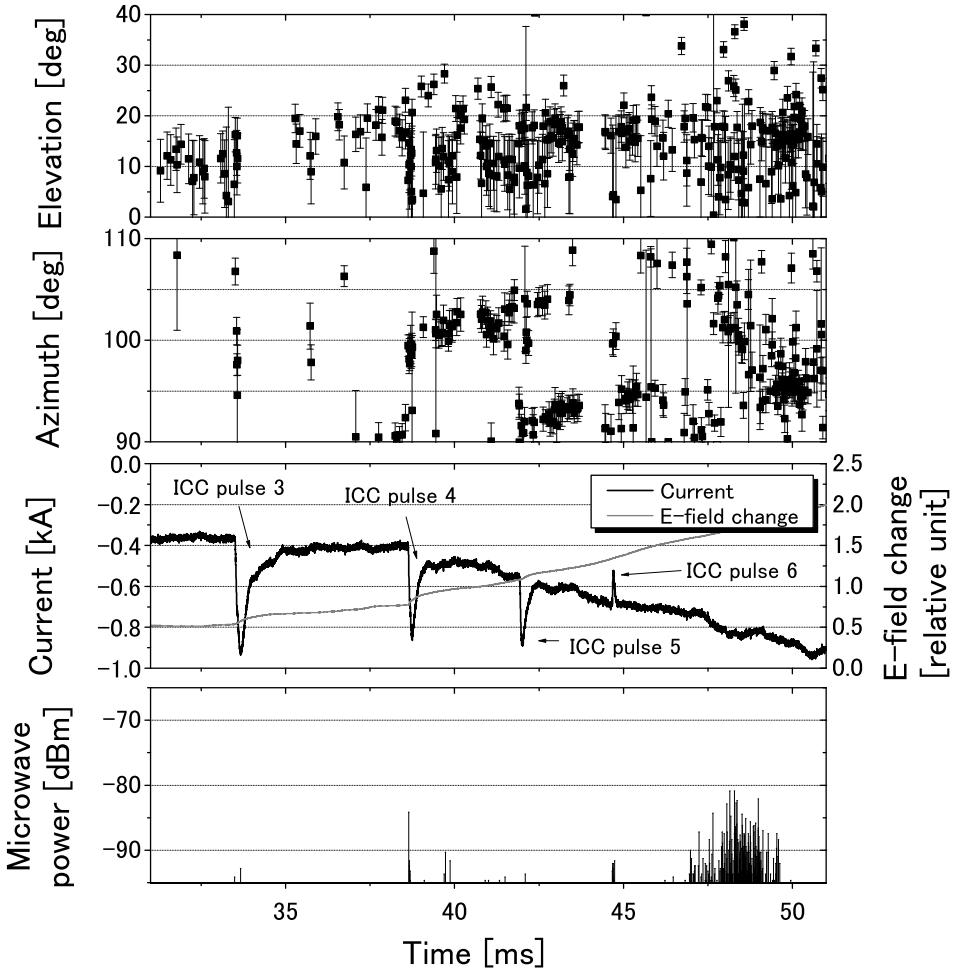

Figure 3.7: The extension of Figure 3.2 between 31 ms and 51 ms. In the third panel, the peaks in the lightning current correspond to the ICC pulses 3, 4, 5, and 6 from the left.

increase in the microwave power was also recorded corresponding to the negative leader development and the peak of the lightning current.

The extension of Figure 3.2 around the ICC pulse 2 is shown in Figure 3.6. Many VHF pulses were located right before the ICC pulse 2, while no VHF radiation is mapped after the ICC pulse 2. The series of VHF radiations is identified as a negative leader since most sources located by the VHF mapper are negative breakdowns (e.g., [34]). This preceding negative leader propagated from 97° to 102° in azimuth. Therefore it also seems that this preceding negative leader connected to the channel of the continuing current. The peak of the lightning current is 11 kA. The charge transfer and the 10-90% risetime in the lightning current for the ICC pulse 2 are 1730 mC and 10 μs, respectively. The bottom

Table 3.1: ICC pulse parameters.

	Polarity	Pulse peak [kA]	Risetime [μs]	HPW* [μs]	CT** [mC]	Preceding leader
ICC pulse 1 (type 1)	negative	25	8	16	665	◯
ICC pulse 2 (type 1)	negative	11	10	6	1730	◯
ICC pulse 3 (type 2)	negative	0.56	102	336	286	×
ICC pulse 4 (type 2)	negative	0.43	74	232	127	×
ICC pulse 5 (type 2)	negative	0.34	42	190	81	×
ICC pulse 6 (type 2)	positive	0.17	28	54	7.9	×
GM*** of type 1	—	17	8.9	9.8	1060	◯
GM of type 2	—	0.34	55	168	69.4	×
GM of all ICC pulses	—	1.3	30	65	172	—
GM of *Miki et al.* [46]	—	0.781	44.2	141	—	—

* The half peak width of the ICC pulse.
** The charge transfer of the ICC pulse.
*** The GM the geometric mean of each parameter.

panel of Figure 3.6 exhibits that the microwave power increases in association with the development of the negative leader and the peak of the lightning current.

Figure 3.7 shows the extension of Figure 3.2 during the period including the ICC pulses 3, 4, 5, and 6. Unlike ICC pulses 1 and 2, no clear negative leader is recognized prior to those ICC pulses in Figure 3.7. The pulse peaks of the lightning current for those ICC pulses 3, 4, 5, and 6 are 0.56 kA, 0.43 kA, 0.34 kA, and 0.17 kA, respectively. In addition the 10-90% risetimes of ICC pulses 3, 4, 5, and, 6 are 102 μs, 74 μs, 42 μs, and 28 μs, respectively. Clear increases in the microwave power corresponding to the VHF radiation from around 100° in azimuth are recognized around 38 ms, 40 ms, 44 ms, and 48 ms. Table 3.1 summarizes the each parameter of the ICC pulses in the flash.

3.5 Discussion

3.5.1 Fast rise ICC pulses

The six ICC pulses are clearly sub-classified into two types according to the pulse shapes. For convenience, these two types of ICC pulses are referred to as type 1 (ICC pulse 1 and 2) and type 2 (ICC pulses 3, 4, 5, and 6). The type 1 ICC pulses have the shorter half peak width and 10-90% risetime, and the higher pulse peak in the lightning current. Meanwhile, the type 2 ICC pulses have the longer half peak width and 10-90% risetime, and the lower pulse peak in the lightning current. Furthermore, the type 1 ICC

pulses have the preceding negative leaders, while the type 2 ICC pulses have no clear preceding leader.

The 10-90% risetime of the ICC pulse 1 and ICC pulse 2 are 8 and 10 μs, respectively. Since the Rogowski coil employed in this study had the pass band between 0.5 Hz and 100 kHz, a current change faster than 10 μs was not be detectable and recorded as a slow change. Therefore the 10-90% risetimes of the type 1 ICC pulses might be shorter than 8 μs and 10 μs. These current peaks and risetimes are quite different from those of the ICC pulses of the triggered lightning reported by *Wang et al.* [44] and similar to the fast rise ICC pulses reported by *Miki et al.* [46].

According to the observation results reported by *Miki et al.* [48], additional luminous channel appeared after the fast rise ICC pulse, while a luminous lightning channel was caused by a continuing current. Also, they assumed that the preceding leaders are needed to create the conducting channel for the fast rise ICC pulse. The preceding negative leader and the type 1 ICC pulses in this study are likely to correspond to the leader prior to the additional luminous channel and the fast rise ICC pulses, respectively, described by *Miki et al.* [48]. Before the type 1 ICC pulses, the charge distribution in the thundercloud was changed significantly by the ICC. The change of the charge distribution brought about a great change in E-field strength around space charges and triggered the preceding negative leaders from the space charge regions. The preceding negative leader developed while creating the conducting channel. After the connection of the preceding leader to the channel of the ICC, the charges of the current of the ICC pulse were transferred through both the channel of the ICC and the conducting channel produced by the preceding negative leaders. The conducting channel created by the preceding negative leader enabled the charge to be transferred very fast as well as return strokes. So, the geometric mean (GM) of 10-90% risetime of the type 1 ICC pulses is much smaller than the type 2 ICC pulses. The sequence of the preceding negative leader and ICC pulse is very similar to the leader - return stroke sequence.

The preceding negative leaders before the type 1 ICC pulses bridged a conducting channel between the space charge region and the existing channel of the ICC. The beginning region of the preceding negative leaders corresponds to the negative charge regions. Most estimated elevations for the negative leaders were located under 15°, which means that the space charge region laid at a height of 700 m or so at most. In addition, the microwave power exhibited apparent increases during the most of the period of the preceding negative leader developments. It means that the preceding leaders propagated mainly within the field of view of the horn antenna. The horn antenna had a narrow beamwidth (30.6° in E-plane and 31° in H-plane) and could detect the microwaves radiation from the height of 400 m from the ground at most. These facts also suggest that the charge regions are located at a very low altitude, namely, at a height of several hundreds meters at most. The previous reports [27, 55] showed that the charge regions in the thundercloud are close to the ground in winter thunderstorm season in Japan. Therefore, the estimated height of these space charge regions reported by this study is possible. Our observation results support the hypothesis presented by *Miki et al.* [46] that the charges transferred by the fast rise ICC pulse are located at the low altitude.

According to the reports [56,57], upward lightning during winter thunderstorm season in Japan can be initiated from rather low grounded-objects than the upward lightning in other locations [41]. The low altitude of space charges, such as the charge transferred by the type 1 ICC pulses, probably is one of the reasons why upward lightning occurs even from low structures during winter thunderstorm season in Japan.

The type 2 ICC pulses do not have clear preceding negative leaders from the direction of the tower prior to the ICC pulses. The type 2 ICC pulses have much longer GM of 10-90% risetime of 55 μs, and longer GM of half peak width of 168 μs than the type 1 ICC pulses. These facts indicate that mechanism of the type 2 ICC pulses is quite different from that of the type 1 ICC pulses. Table 3.1 indicates that the GM values of the type 2 ICC pulses have similar characteristics reported by *Miki et al.* [46]. Therefore the type 2 ICC pulses are probably "typical" ICC pulses, although the details of the type 2 ICC pulses have not been clarified yet.

3.5.2 Microwave radiations associated with lightning

The pulses in the microwave radiations are also sub-classified into two types, a short duration and a long duration. One typical example is seen in Figure 3.8, which is the extension of Figure 3.5 between 6.48 ms and 6.68 ms. Most of the microwave power pulses between 6.48 ms and 6.6 ms have short duration less than 1 μs while the duration of the microwave power corresponding to the ICC pulse 1 is 16 μs and 26 μs. The short duration pulses of the microwave power appeared simultaneously with the negative leader development. Another example is seen between 47 ms and 50 ms in Figure 3.7. The second panel of Figure 3.7 shows that a negative leader developed from the direction of 105° to 95° in azimuth during this period. A train of the increases in the microwave power corresponds to the leader development. The train consists of short duration pulses of the microwave power. Because the typical duration of VHF pulses radiated from the negative leader is less than 640 ns [9], these short pulses in the microwave power probably were components of those impulsive pulses radiated from the tips of the negative leaders. In other words, the charge movement in short distance at the tip of the negative leader radiated 2.9 GHz impulsive electromagnetic waves as well as VHF electromagnetic waves detected by the VHF broadband DITF.

On the other hand, the long duration microwave pulses seem to correspond to the current pulse. The waveform of the microwave power has two peaks accompanied by the current increase and the E-field change. The third panel of Figure 3.8 shows the peak power of all VHF pulses recorded by the VHF broadband DITF at that time. No VHF pulse was recorded during the long-duration microwave increases. The dead time of the VHF broadband DITF was less than 1 μs. The long-duration microwave power increases were not accompanied by VHF radiations, which means that no impulsive phenomena, such as negative leader developments, occurred nearby at that time. Other examples are seen in Figures 3.4 and 3.6. The long duration pulses in the microwave power correspond to the peak current of the UPL and ICC pulse. These clear increases in the microwave power, the current increase, and the abrupt E-field change occurred simultaneously. It

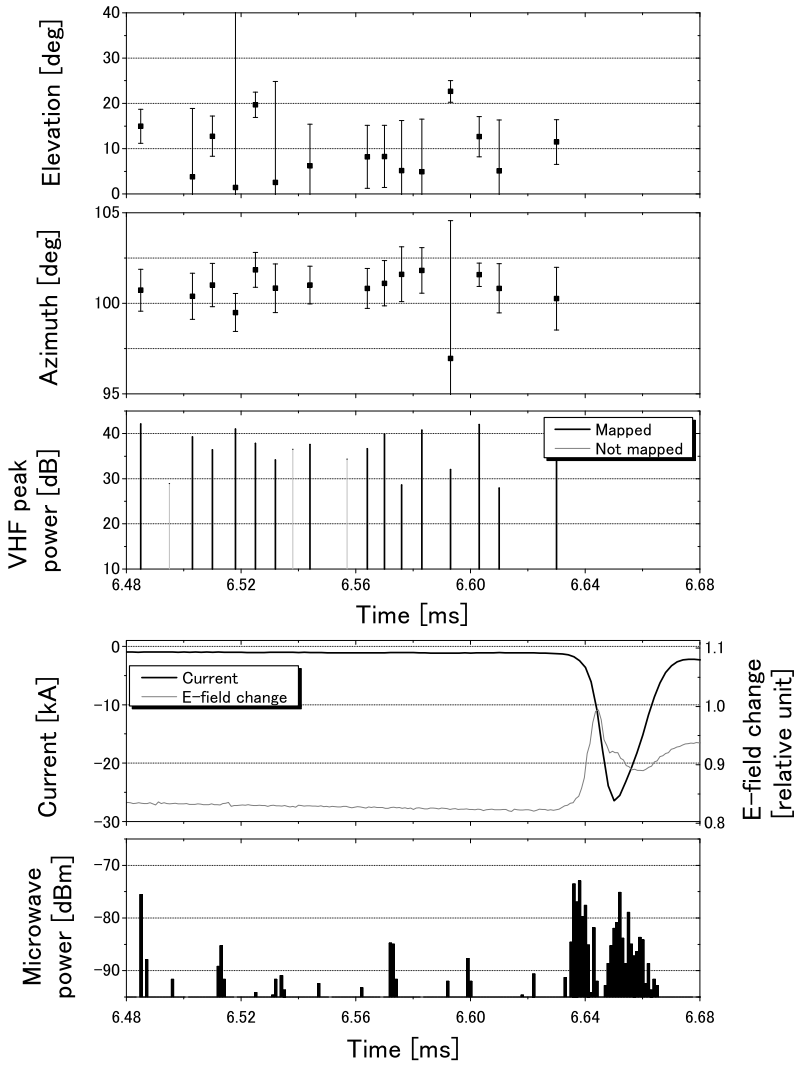

Figure 3.8: The extension of Figure 3.5 between 6.48 ms and 6.68 ms. The top, second, fourth, and bottom panels correspond to the top, second, third, and bottom panels in Figure 3.2, respectively. The third panel shows the peak power of the VHF pulses detected by the VHF broadband DITF. The "Mapped" peak VHF power indicates the VHF peak power of the electromagnetic waves whose directions are estimated in terms of elevation and azimuth, while the "Not mapped" VHF peak power indicates the VHF peak power of the electromagnetic waves whose directions are not be estimated.

seems that these apparent increases were caused by the large lightning current caused by the UPL and the ICC pulses. These results are consistent with the previous reports [50].

One possible source of these long duration 2.9 GHz radiations is thermal emissions

from the channel of the lightning current. The temperature of return strokes was estimated up to 30,000 K [11]. The temperature of the ICC pulses and UPL might be several ten thousands Kelvin. To prove this assumption, further observations and discussions are needed.

3.6 Summary

A lightning observation campaign was conducted during winter thunderstorm season in Japan, which borders the Sea of Japan. This observation campaign aimed to study the fast rise ICC pulses in the IS as well as the microwave radiation associated with the upward lightning. We showed one upward negative lightning, including one upward leader and six ICC pulses. The six ICC pulses are sub-classified into two types. In this study we focus on the type 1 ICC pulse, which has the short 10-90% risetime in the lightning current. The negative leader developments were recognized prior to the type 1 ICC pulses. It seems that these preceding negative leaders created the conducting channel that caused the ICC pulse. In addition, the estimated height of the charge region transferred by the ICC pulse 1 was around 700 m from the sea level at most. These facts support strongly the hypothesis described by *Miki et al.* [46, 48]. They speculated that the fast rise ICC pulses are caused by the sequence similar to leader - return stroke. Also, they assumed that the charges removed by the ICC pulse were located at very low altitude.

The waveforms of the microwave power exhibited apparent increases from the background level. The observation results implied that the negative leader developments and lightning current have detectable microwave radiations. Though the results in this study are preliminary, and further investigation and more evidence are needed, the observation results imply a possibility of a new lightning mapping system by means of microwave emissions.

Chapter 4

Analysis of the LIS data on the TRMM

4.1 Introduction

In this chapter, analyses of the Lightning Imaging Sensor (LIS) data on the Tropical Rainfall Measuring Mission (TRMM) are presented. The TRMM is an earth observation satellite on which five installments are operated. The main missions of the TRMM are to conduct global scale rainfall observations including tropical ocean regions, where observation points are rare, and to investigate rainfall mechanisms. In this chapter we employ the Precipitation Radar (PR) and the LIS on the TRMM. Two main subjects are then discussed: one is the parameterization of lightning activity (in Section 4.2) and the other is the relationship between lightning activity and the El Niño Southern Oscillation (ENSO) events (in Section 4.3). Finally, all contents in this chapter are summarized in Section 4.4.

4.2 A universal fifth power law of lightning activity

4.2.1 Background

Knowledge of global lightning activity has grabbed the researchers' attentions to examine the changes of it as a result of global warming [60] and the El Niño Southern Oscillation (ENSO) events [61–63]. Furthermore, in the field of atmospheric chemistry, in order to estimate the global NO_x precisely, the global lightning data was used for in the parameterization (e.g., [64]), since the lightning flash is one of the major sources of NO_x on our planet [65].

To estimate the number of lightning flashes all over the world, a parameterization has been attempted using some thundercloud parameters such as updraft speed, precipitation, and storm height [66–70]. Recently, a "fifth power law", which is the relationship that the flash rate is proportional to the fifth power of the storm height has been investigated [66].

Williams [66] simplified the basic Vonnegut's idea [71] and suggested a simple relationship that the flash rate is proportional to the fifth power of the thunderstorm under the following four assumptions: (1) The charge density within the thunderstorm is inde-

pendently of the thunderstorm size, (2) the thunderstorm has a scale similarity between vertical and horizontal scales, (3) the updraft velocity is proportional to the storm height, and (4) the flash rate is proportional to electrical generator within the thundercloud. Then, *Williams* [66] shows the fifth power relationship as a result of the field observations in Florida [72, 73], New Mexico [66], and New England [74]. The observation results were in very good agreement with the results of the scaling laws. Very little attention, however, was given to lightning activity on the ocean since the observations were based on the land.

Price and Rind [67] considered the difference of the updraft velocities between on the land and the ocean to improve the relationship derived by *Williams* [66]. They applied their relationships to estimate global lightning distributions. They estimated the flash rate from the storm height measured by International Satellite Cloud Climatology Project (ISCCP) over the land and the ocean. Then, *Price et al.* [75] estimated the global NO_x production by lightning.

Michalon et al. [68] took into account the effect of the droplet concentration on charge separation in the thundercloud. They asserted that the flash rate is proportional to the fifth power of the cloud top not only on the land but also on the ocean based on the results of the previous work [67]. The annual distribution of lightning activity all over the world was estimated from General Circulation Models (GCMs) with their parameterizations. Furthermore, they estimated a roughly 2°C increase in surface may cause a 10% increase of global annual flash frequency.

Boccippio [76] and *Ushio et al.* [69], however, showed negative results to the previous works. *Boccippio* [76] examined the assumptions in the previous paper [67] based on *Vonnegut*'s theory [71] and asserted that their assumptions in their parameterization over the ocean should be improved from a theoretical standpoint. *Ushio et al.* [69] analyzed the data from the TRMM during one month over the land and the ocean, and concluded that the flash rate increases exponentially with the storm height. This implies that it is not proportional to the fifth power of the storm height because the thundercloud formation mechanisms over the land and the ocean are different. Therefore, they proposed that other parameters or reexamination must be taken into account to parameterize the flash rate.

Although the fifth power law has been examined through several case studies on the basis of ground observations [66] and satellite observations [69], we do not have a unified view about it. One reason is that their analyses involved a couple of problems associated with the definitions of the parameters. First, the storm height is used as a thundercloud parameter. The storm height is defined as a radar echo top height, and it is not directly associated with the amount of graupel and ice crystals that cause the charge separations in the convective cloud [77–79], because the storm height includes the altitude below the freezing level. Therefore the storm height is not directly associated with lightning activity and should not be employed for the parameterization.

Secondly, the flash rate was employed as a lightning activity parameter. The flash rate is given as the number of flashes per a minute per a convective cloud with flashes during the scan time of the LIS [69]. If a convective cloud has no lightning flash during the observation time, the convective cloud is not included in their statistics. However, if a

convective cloud has a great deal of graupel and ice particles in it, the convective cloud has the likelihood of making lightning occurrence. The likelihood of flashes is not included in the definition of the flash rate because they ignore the convective cloud without lightning flashes during the scan time of the LIS.

To resolve the problems of the previous works (e.g., [66]) two modifications are applied. First we introduce the snow depth, which is defined as the difference between the freezing level and the echo top height. Because the snow depth is directly associated with the volume of the graupel and ice particles, it should be related to the lightning activity. Secondly, we also introduce Number of lightning Flashes per Second per Convective cloud (NFSC). The NFSC is defined as the number of flashes divided by the total observation time of the convective clouds detected all over the observation periods. In this study, the TRMM data throughout eight years are employed to examine the relationship between the NFSC and the snow depth. This analysis period and the areas covered by the TRMM are large enough to process statistically. We show the relationship between the NFSC and the snow depth under several conditions and discuss the parameterization of lightning.

4.2.2 Methodology

In this study, we used data sets obtained from the PR and the LIS on the TRMM, which was launched into a 35 degree inclination orbit on the 28th of November in 1997. The PR is a spaceborne radar operating at 13.796 and 13.802 GHz and has 4.3 km horizontal and 250 m vertical resolution over a 220 km swath, with the minimum detectable Z $\sim$16-18 dBZ, considering the system noise and signal-to-noise ratio (S/N) [59] (see

Table 4.1: The specifications of the PR.

Precipitation Radar (PR)	
Frequency	13.796 & 13.802 GHz
Swath width	220 km
Vertical Resolution	250 m
Horizontal Resolution	4.3 km

Table 4.2: The specifications of the LIS.

Lightning Imaging Sensor (LIS)	
Band	777.4 nm
Swath width	600 km
Horizontal Resolution	4 km

Table 4.1). The PR have provided monthly and annual precipitation data. The LIS on the TRMM detects optical emissions from both in-cloud and CG lightning [12], and it locates lightning flashes that occur within its 600 $\times$ 600 km^2 field of view (FOV), a nadir pixel resolution of 4 km (see Table 4.2). The average view time of the LIS is 79 sec before the TRMM boosting on August 2001 and 93 sec after that.

We introduce the snow depth and the NFSC as new parameters. The snow depth is defined as the difference between the echo top height and the freezing level. Therefore the snow depth (D) is calculated from the storm height (H) and the estimated height of the freezing level (F) provided by the PR.

$$D = H - F. \tag{4.1}$$

In this study, the largest D in a convective cloud is employed for statistical analyses. The definition of the convective cloud will be shown later. The snow depth is rounded off in kilometers. We also introduce the NFSC as a lightning parameter to estimate the likelihood of lightning activity in the convective cloud. Let $N(D)$ denote the number of convective clouds with D km in the snow depth recorded by the PR. For example, it is assumed that the ith convective cloud with the snow depth D has L_i flashes located by the LIS. The scan time of the ith convective cloud by the LIS is t_i sec. The NFSC is defined as follows,

$$NFSC(D) = (\sum_{i=1}^{N(D)} L_i)/(\sum_{i=1}^{N(D)} t_i). \tag{4.2}$$

In the case of this study, since $N(D)$ is enough large, the following approximation can be applied.

$$NFSC(D) \approx (\sum_{i=1}^{N(D)} L_i)/(T \times N(D)), \tag{4.3}$$

where T denotes the average scan time of the LIS. The average scan time of the LIS is 79.1 sec before the TRMM boosting on August 2001 and 92.2 sec after that. That is to say, under several conditions, we count the number of convective clouds with D km in the snow depth ($N(D)$) and the number of flashes located by the LIS in these convective clouds ($\sum_{i=1}^{N(D)} Li$). After that, the number of flashes is divided by the product of $N(D)$ and the average scan time T of the LIS. In analysis periods, some NFSCs are eliminated when the NFSCs has $N(D)$ less than 200 and the number $\sum_{i=1}^{N(D)} Li$ of flashes located by the LIS less than 100 from the analysis because the approximation should not be applied.

Lastly, the definition of convective clouds is shown. The 2A23 PR product provides rain type that distinguishes whether the cloud is stratiform or convective. In this study, if at least two successive pixels are recognized as convective and the all successive pixels are included in the PR track, the minimum rectangle containing those pixels is defined as a convective cloud. Therefore, a huge convective cloud like a super cell, which has over 220 km in horizontal scale, and the flashes occurred in those convective clouds are

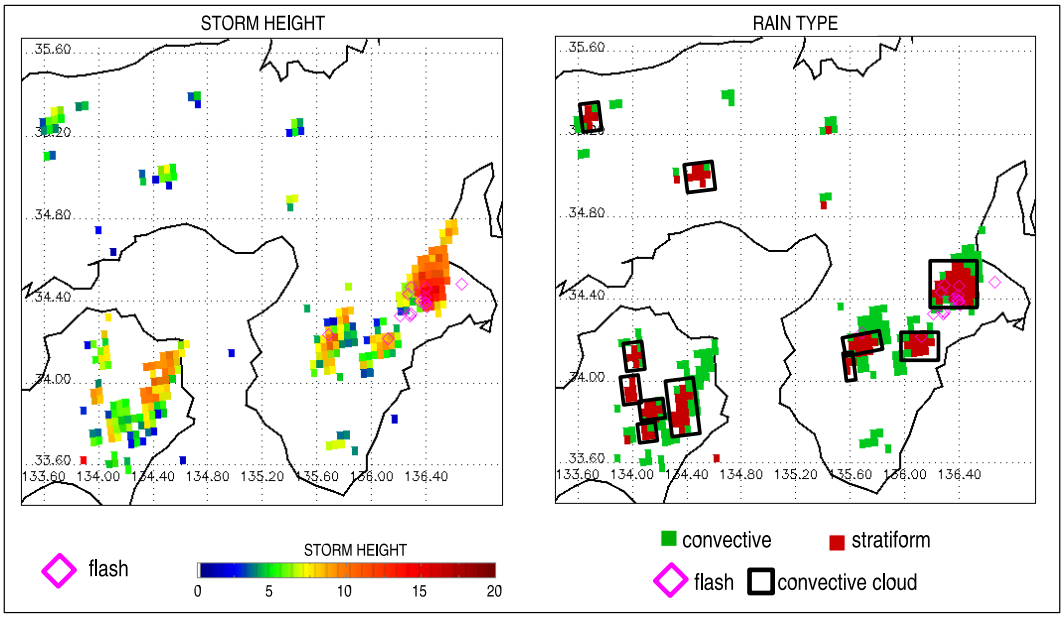

Figure 4.1: An example of the definition of convective clouds. These convective clouds and flashes were observed on the 14 of July on 2001 by the PR and the LIS on the TRMM. Almost all flashes were recognized in the defined convective clouds.

not included in the analyses because the PR has a 220 km swath. The convective clouds with a horizontal scale of 8 - 215 km are involved in this analyses. Figure 4.1 shows an example for the definition of convective clouds. In the figure, eleven convective clouds are recognized and almost all flashes located by the LIS occurred in the defined convective clouds.

In this study, we have an assumption that NFSC is proportional to the power of the snow depth.

$$NFSC = 10^{\beta} \times D^{\alpha}. \tag{4.4}$$

Here, α and β in the formula (4.4) are determined statistically in this study. The α and β are termed an exponent factor and a coefficient factor, respectively. During analysis peri-

Table 4.3: Summary of analysis.

Analysis period	1998 - 2005
The number of the convective clouds	8.61×10^6
The number of the flashes on the PR track	3.09×10^6
The number of the flashes in the convective clouds	2.49×10^6
Percentage of the flashes in the convective clouds	80.8 %

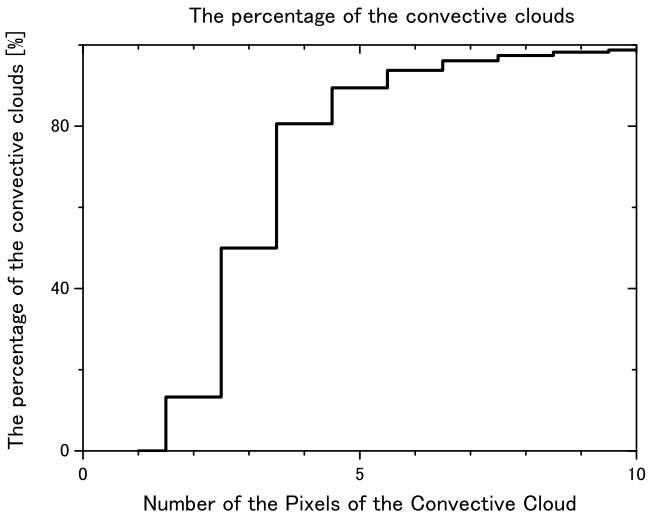

Figure 4.2: The cumulative distribution of the horizontal scale of the convective clouds in this analysis. Most convective clouds have 4 or less pixels in the horizontal scale.

ods, the exponent factors and coefficient factors are calculated under several conditions.

The data from January 1998 to December 2005 are used. Table 4.3 summarizes the analysis. The number of the convective clouds and flashes detected by the LIS on the orbit of the PR are more than 8.6 million and 2.4 million, respectively. They are large enough to process statistically. Moreover, the percentage of the flashes located by the LIS within the defined convective clouds exceeds 80%. This is a piece of evidence for the validity of the definition method of the convective clouds in this study. Figure 4.2 shows the cumulative distribution of the horizontal scale of convective clouds in this analysis. This figure shows more than 80% convective clouds defined in this analysis have 4 or less pixels in the PR, which means horizontal scales of most convective clouds are less than 16 km. These results are consistent with the facts that the horizontal scale of most thunderstorms is 10 km or so (e.g., [80]). Thus these facts also support the validity of the convective cloud definition.

4.2.3 Results

Figure 4.3 shows the relationship between the NFSC and the snow depth in the double logarithmic chart all over the detection area of the TRMM for whole 8 years. It is found out that the figure shows the linear relation in the logarithmic scale. The exponent factor and the coefficient factor are 5.0 $\pm$0.1 and -6.2 $\pm$0.1, respectively. In this study, the errors mean their standard deviations. Only the relationship up to 12 km in the snow depth is shown because the detection efficiency for flashes, especially CG flashes, decreases

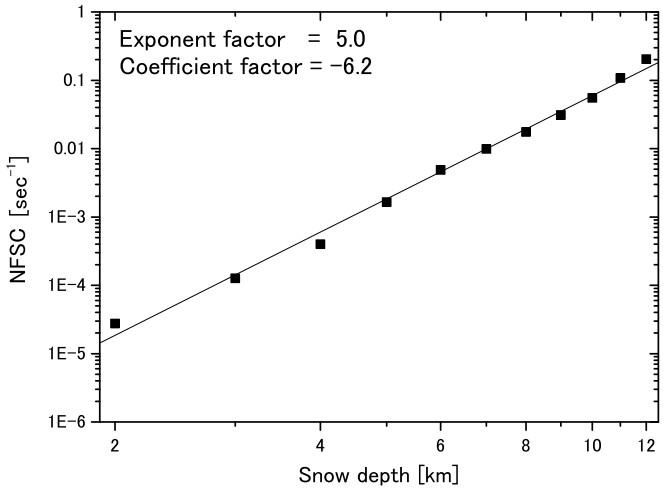

Figure 4.3: The correlation between the NFSC and the snow depth for whole eight years and all over the detection area of the TRMM (from around 35°S to 35°N).

drastically for the storms with 13 km or more of the snow depth. Figure 4.4 shows the number of convective clouds, the number of the convective clouds with flashes located by the LIS, and the rate of the number of the convective clouds with flashes located by the LIS to the number of the convective clouds against the snow depth. Many investigators reported that a higher cloud top causes higher flash rate (e.g., [81]), so the higher snow depth should cause higher rate with flashes. In Figure 4.4, the rate increases up to 12 km in the snow depth, while the rate decreases over 13 km in the snow depth. According to the previous reports [82, 83], the detection efficiency of the LIS is low for flashes occurred in the lower altitude of the thundercloud because of thickness in the optical depth. It seems that the thick cloud depth above 13 km in the snow depth decreases the LIS detection efficiency for flashes. That is why the large snow depth is eliminated in this study. In the whole 8-year analysis all over the TRMM observation areas, the NFSC is proportional to the fifth power of the snow depth.

We conduct the analysis to investigate the regional dependency under the definition of regional boundaries shown in Table 4.4 and Figure 4.5. The lands, the oceans, and the coast are clearly classified in this division. Any oceanic region is at least 5° far from any continents. The oceanic areas have enough distance from any land, so continents do not have any effect on the oceanic area. Figure 4.6 shows the similar plots with Figure 4.3 but for all regions shown in Figure 4.5.

First, the NFSCs are proportional to the snow depth in the double logarithmic scale independent of the region since their linear regression lines are almost parallel. In other words, the exponent factors are fairly constant and independent of the region, although it

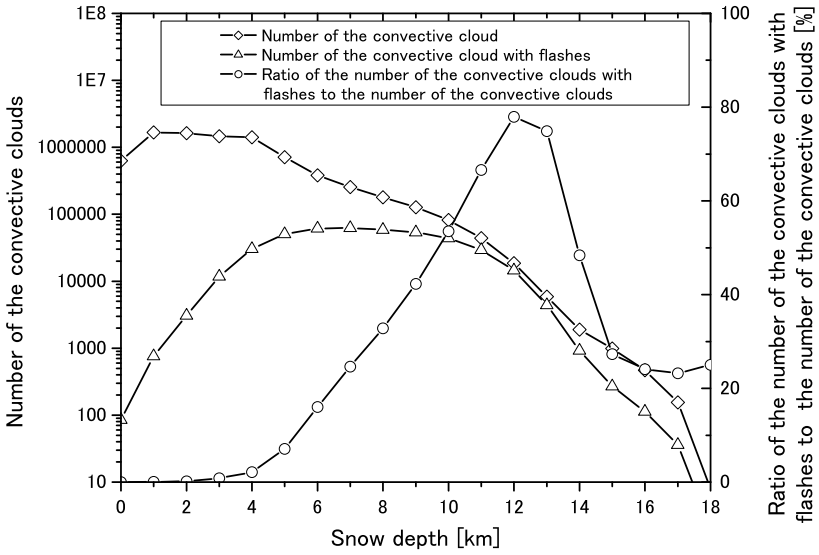

Figure 4.4: The diamonds ($\diamond$) and the triangles ($\triangle$) correspond to the number of the convective clouds and the number of the convective clouds with flashes located by the LIS (the left axis), respectively. The circles ($\bigcirc$) correspond to the ratio of the number of the convective clouds with flashes located by the LIS to the number of the convective cloud (the right axis).

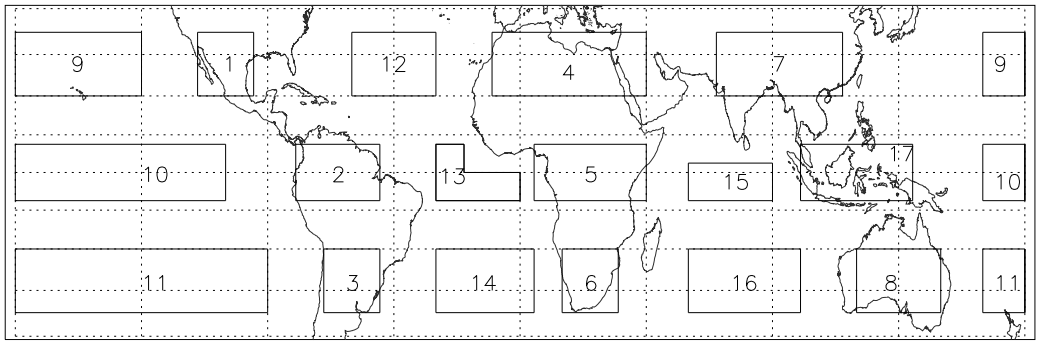

Figure 4.5: Study region boundaries. The regions from 1 to 8, from 9 to 16, and 17 correspond the lands, the oceans, and the coast, respectively. See also Table 4.4.

was believed in the previous papers [67, 69] that the best fit power law relationships vary with location. The average exponent factors are 5.0 ± 0.4 for the lands and 5.0 ± 0.6 for

Table 4.4: Study region boundaries.

Region No.	Land/Ocean/Coast	Latitudes	Longitude
1	Land	20° - 35°N	95° - 115°W
2		7.5°S - 7.5°N	50° - 80°W
3		35° - 20°S	50° - 70°W
4		20° - 35°N	10°W - 45°E
5		7.5°S - 7.5°N	5° - 45°E
6		35° - 20°S	15° - 35°W
7		20° - 35°N	70°W - 115°E
8		35° - 20°S	120° - 150°W
9	Ocean	20° - 35°N	165°E - 135°W
10		7.5°S - 7.5°N	165°E - 105°W
11		35° - 20°S	165°E - 90°W
12		20° - 35°N	60°W - 30°W
13		7.5°S - 7.5°N	30°W - 0°
14		35° - 20°S	30°W - 5°E
15		7.5°S - 2.5°N	60°E - 90°E
16		35° - 20°S	60°E - 100°E
17	Coast	7.7°S - 7.5°N	100°E - 140°E

See also Figure 4.5. The region (0° - 7.5°N and 20°W - 0°) was eliminated from Region No. 13.

the oceans, respectively. Furthermore, the exponent factor for the coast is 5.2. Therefore there is no significant deference in the exponent factor among regions. The NFSCs are almost proportional to the fifth power of the snow depth without regional dependencies.

Secondly, most NFSCs of the land are larger than those of the ocean. The NFSC of the coast region lies approximately between those of the lands and the oceans. This is consistent with the previous findings that the lightning activity over the ocean is lower than that on the land [60,84,85]. The average coefficient factors are -5.9$\pm$0.4 for the lands and -7.0$\pm$0.9 for the oceans, respectively. The coefficient factor for the coast is -6.7. The average coefficient factor for the land is larger than that for the ocean approximately by one. This indicates that convective clouds on the land have nearly 10 times more lightning flashes than those on the ocean even if they have the same snow depth. Roughly speaking, this fact is coincident with the report [86] that lightning occurs mainly over land with an average land/ocean ratio of around 10.

To examine the seasonal dependencies, we conduct the same analysis for the four seasons, that is, from March to May (MAM), from June to August (JJA), from September to November (SON), and from December to February (DJF). Each panel of Figure 4.7 shows the correlation between the NFSC and the snow depth in each region with the same format as in Figure 4.6. Because of the less numbers of the convective clouds and flashes,

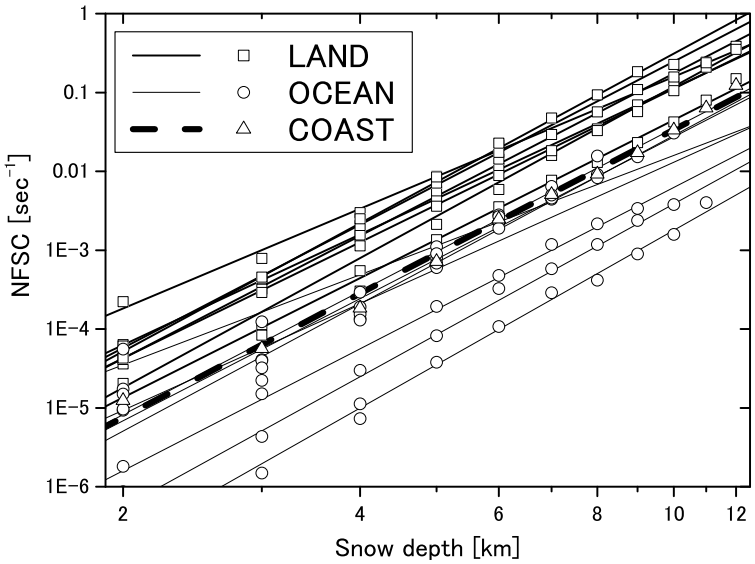

Figure 4.6: The correlation between the NFSC and the snow depth in each region for whole eight years with the same format as Figure 4.3.

Table 4.5: Average of each parameter in each season.

Region	Season	Exponent factor	Coefficient factor
Land	DJF	5.0 ± 0.4	-5.8 ± 0.6
	MAM	5.2 ± 0.4	-6.0 ± 0.5
	JJA	5.1 ± 0.5	-5.9 ± 0.4
	SON	5.1 ± 0.5	-5.9 ± 0.4
Ocean	DJF	5.4 ± 0.5	-7.3 ± 1.0
	MAM	5.2 ± 0.3	-7.1 ± 0.6
	JJA	5.4 ± 0.5	-7.3 ± 1.0
	SON	5.3 ± 0.4	-7.3 ± 0.9
Coast	DJF	5.2	-6.8
	MAM	5.1	-6.6
	JJA	5.4	-6.8
	SON	5.2	-6.6

the exponent and coefficient factors are not calculated in some conditions, namely the region number 14 in the panel of MAM, 13 in the panel of SON, and 13, 14, 16 in the

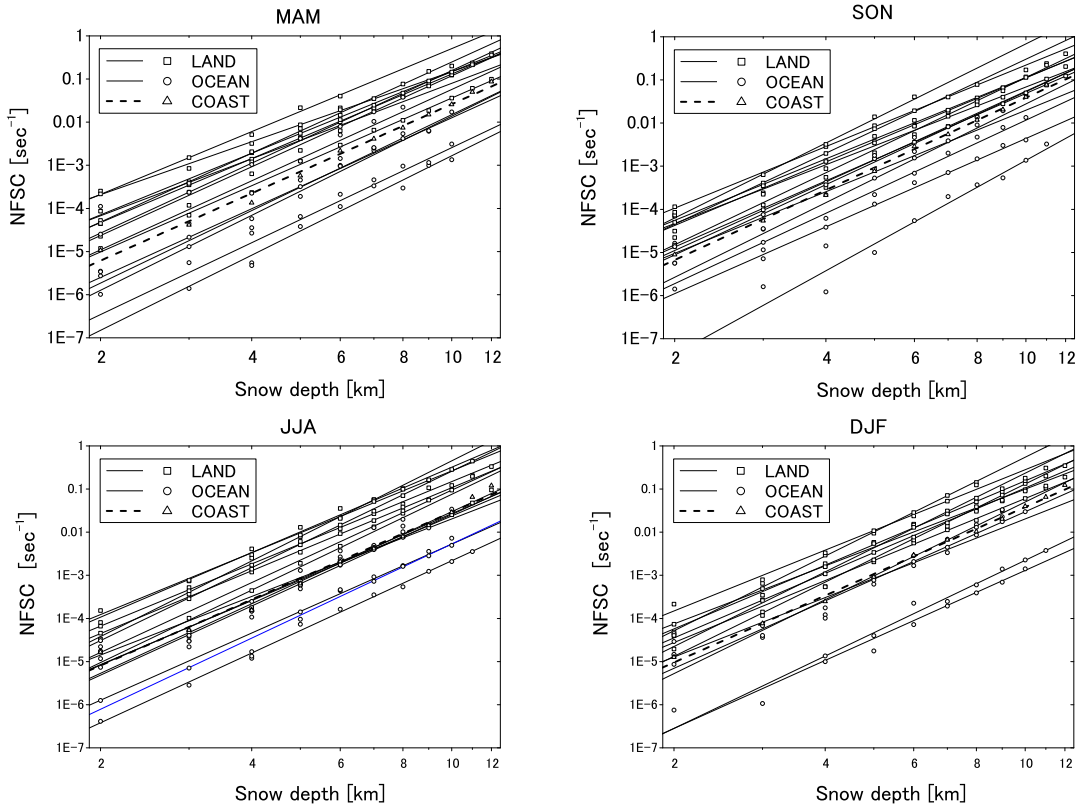

Figure 4.7: The correlations between the NFSC and the snow depth in each region for all four seasons with the same format as in Figure 4.6.

panel of DJF. The NFSCs are proportional to the snow depth and their regression lines seem to be parallel in each season as well. There is no significant difference among these panels in Figure 4.7. Table 4.5 shows the averages of the exponent and coefficient factors in each season. These results indicate that both the exponent factors and the coefficient factors are independent of the seasons. The exponent factors are almost five. When we focus on only the regional dependencies, regardless of the seasons, the average exponent factors are 5.1 ± 0.4, 5.3 ± 0.4 , and 5.2 ± 0.1 for the lands, ocean, and coast, respectively. In other words, most exponent factors are almost five independently of region and season. The NFSCs in the lands exceed them in the oceans and the NFSCs in the coast lie between the lands and the oceans in Figure 4.7.

Finally, we conclude that the NFSC is proportional to the fifth power of the snow depth irrelevant to any region and season. Moreover, the difference between the land and the ocean affects not the exponent factors but the coefficient factors.

4.2.4 Discussion

To confirm the results discovered statistically, there are two scenarios to interpret. If we have a reasonable assumption that electric energy consumed by a flash is constant, a convective cloud with greater electric energy in it has more lightning activity in it. In other words, the electric energy in the convective cloud is proportional to the NFSC (Scenario 1). If we have another reasonable assumption that the charge neutralized by each lightning stroke is constant, the charge generated in the convective cloud is proportional to the NFSC (Scenario 2). The details of the two scenarios will be shown in turn.

Scenario 1

In this discussion, the electro-static energy stored in a convective cloud is calculated. We have learned the charge distribution inside the convective cloud is more complicated than we expected (e.g., [87]). That means not only a dipole model but also a tri-pole one are still insufficient. In the most active stage of a thundercloud, the electric charge distribution may be more than five or six layers. However, to make the problem simple we dare to introduce the dipole model in this discussion, and the followings are the principle assumptions.

(A) The dipole thundercloud model is applied.

(B) The electric field in the convective cloud is vertical and scale independent.

(C) The distance of the positive and negative charge centers is proportional to the snow depth D.

(D) The total volumes where charged graupel and ice particles exist are proportional to D^3.

(E) The NFSC is proportional to the static energy of the electric dipole in the convective cloud.

With assumptions (A), (B), (C), and Gauss' law, the electro-static energy W is proportional to the product of the positive and negative charge quantities, and inverse proportional to the distance of the charge centers.

$$W = A\frac{Q_p Q_n}{D}, \tag{4.5}$$

where, A, Q_p, Q_n are a constant, the positive and negative charge quantities in the convective cloud, respectively. The formula (4.5) is transformed into the formula (4.6) with assumption (D),

$$W = A' q_p q_n m_p m_n D^5, \tag{4.6}$$

because $Q_p \propto q_p m_p D^3$ and $Q_n \propto q_n m_n D^3$. Here, A', q_p (q_n), and m_p (m_n) are a constant, the mean positive (negative) electrical charges of individual cloud particles, and the mass

densities of the positively (negatively) charged region, respectively. Since the q_p, q_n, m_p, and m_n are intensive, they should be scale independent. It follows from assumption (E) and the formula (4.6) that

$$NFSC \propto W = A''D^5. \tag{4.7}$$

Here, A'' is a constant and scale independent. The formula (4.7) means that the NFSC is proportional to the fifth power of the snow depth. The constant A'' represents the dependency on the mass densities m_p and m_n in the convective clouds. Since the rebounding graupel-ice crystal collisions cause the lightning electric charge separation (e.g., [77]), a vigorous charge separation needs a great deal of ice particles. The ice water path, which corresponds to the ice water mass in the convective cloud, on the land is mainly much higher than that on the ocean [70]. Then, the mass densities m_p, m_n on the ocean are lower than those on the land. Therefore the constant A'' on the oceans is lower than that on the lands.

Scenario 2

In this discussion, we calculate the temporal differentiation (dQ/dt) of electric charge generated in a convective cloud, which should be proportional to the NFSC. According to the previous reports [88–90], the differentiation is proportional to the product of downward flux of the solid precipitation and the upward flux of ice particles in a charging zone where the collisions between graupel pellets and ice particles occur. We have six assumptions as follows.

(F) dQ/dt is proportional to the product of downward flux of the solid precipitation and the upward flux of ice particles in the charging zone.

(G) The base of the charging zone defined as a rectangular solid is proportional to the D^2.

(H) The depth of charging zone is scale independent.

(I) The terminal velocity of the solid precipitation in the charging zone is scale independent.

(J) The upward velocity of ice particles in the charging zone is proportional to the D.

(K) dQ/dt is proportional to the NFSC.

From assumption (F),

$$dQ/dt = BpF_i. \tag{4.8}$$

Here, B, p, and F_i are a constant, the downward flux of the solid precipitation, and the upward flux of the ice particles, respectively. The shape of the charging zone is "like a pancake", and the depth of the charging zone is less than 1 km [91]. The depth of the

charging zone can be scale independent. With assumptions (G) and (H), the formula (4.8) is transferred into the formula (4.9).

$$dQ/dt = B' M_p M_i D^4 V U, \tag{4.9}$$

because $p = M_p D^2 V$ and $F_i = M_i D^2 U$, here, B, M_p, M_i, V, U are a constant, the mass density of precipitable particles, the mass density of ice particles, the average terminal velocity of the precipitable particles, and the average updraft velocity of the ice particles, respectively. To make the discussion simple, the average terminal velocity V is presumed to be scale independent with the assumption that the size of precipitating particles in the charging zone is scale independent [92]. Then with assumptions (I) and (J) the formula (4.9) is transferred into the formula (4.10).

$$dQ/dt = B'' D^5, \tag{4.10}$$

here, B'' is a constant and scale independent. Then with assumption (K) the formula (4.10) is transferred into formula (4.11).

$$NFSC \propto dQ/dt = B'' D^5. \tag{4.11}$$

The formula (4.11) also means that the NFSC is proportional to the fifth power of the snow depth. Furthermore, B'' depends on the product of the mass densities of precipitable particles and ice particles. Therefore, since the convective clouds on the lands have much more precipitable particles and ice particles (e.g., [70]), B'' in the formula (4.11) on the land are greater than that on the oceans. Finally, these simple dimensional analyses agree with the results of the TRMM observation.

4.3 Relationship between lightning activity and ENSO events

4.3.1 Background

The El Niño Southern Oscillation (ENSO) is a well recognized feature of the ocean-atmosphere system in the Tropical Pacific. It is known that the major impact of the sea surface temperature (SST) change during the El Niño event is the shift in convection from the western to the central and the eastern Pacific Ocean, thereby affecting the response of rain-producing cumulonimbus. *Rasmusson and Carpenter* [93] reported that the ENSO event may impact the Asian-Australian monsoon. These atmospheric circulation changes during ENSO events could influence storm frequency and intensity [60, 94], and connections have been found between lightning activity and ENSO events in various regions [62].

The 1997-1998 El Niño event, which began to develop in March 1997 and strengthened rapidly, was one of the strongest El Niño events. After a gradual decline in the intensity of these thermal anomalies in early 1998, the El Niño event abruptly ended during July-August 1998. A La Niña event started soon after this strongest El Niño event. This La Niña event continued more than a year, and then disappeared in the spring of

2000. *Hamid et al.* [61] asserted that during the El Niño period, lightning was more frequent despite fewer convective storms in Indonesia. In this study, first we focus on my attention on the relationship between Southern Oscillation Index (SOI) and the lightning activity in East/South-East Asia Region (EAR; 90°-130°E, 10°S-40°N) including Indonesia. Secondly we investigate the contrast of the convective activity between El Niño and La Niña periods over the Western Pacific Region (WPR; 60°-160°E, 40°S-40°N), which includes EAR.

4.3.2 Methodology

In this study, we used data sets provided by the Tropical Rainfall Measuring Mission (TRMM) and the NCEP/NCAR Reanalysis Project. The data of precipitation, radar reflectivity, and lightning discharge are obtained from Precipitation Radar (PR) and Lightning Imaging Sensor (LIS) on the TRMM. The PR data we used are the 3A25 (version 2) PR products which provide monthly atmospheric parameters such as total and conditional rain rates and radar reflectivity for each 5° and 0.5° grid. In this product, we employ the 0.5° monthly average of the radar reflectivity for convective clouds at a height of 6 km and the rain count defined as the number of detections of precipitation at a height of 2 km by the PR. We defined flash rates which were normalized with view time of LIS for each 1° grid. The data of wind velocity and sea level pressure are obtained from the NCEP/NCAR Reanalysis Project. From this project, we used the monthly mean of the U-wind (the latitudinal wind velocity), V-wind (the longitudinal wind velocity), and sea level pressure at the surface or near the surface level. Moreover we also used the Southern Oscillation Index (SOI) defined as normalized sea-level pressure difference between Tahiti and Darwin [95].

We studied the data from January 1998 to December 2003. During this period, two El Niño and one La Niña events are recognized. The first El Niño event occurred from the spring of 1997 to the summer of 1998, and the second is from the spring of 2002 to the winter of 2002/2003. The La Niña event occurred from the autumn of 1998 to the spring of 2000. In this study we defined the El Niño period from January to August 1998 and from March 2002 to February 2003, and the La Niña event from September 1998 to May 2000.

4.3.3 Results

It was reported that lightning activity over Indonesia during the El Niño period was more frequent than during the La Niña period as a result of 2-year analysis by *Hamid et al.* [61]. To clarify this relationship, we expand the analysis period into six years. Figure 4.8 shows the monthly variation of SOI and the variation of the flash rate in EAR from 1998 to 2003. Here, the variation of the flash rate is represented by the rate of variability from the six-year average. Though the index of correlation between SOI and the variation of flash rate is -0.43 for all six years, it is -0.61 when we focus on only the El Niño and La Niña events. Furthermore it is noticeable that during the period from January 1998 to

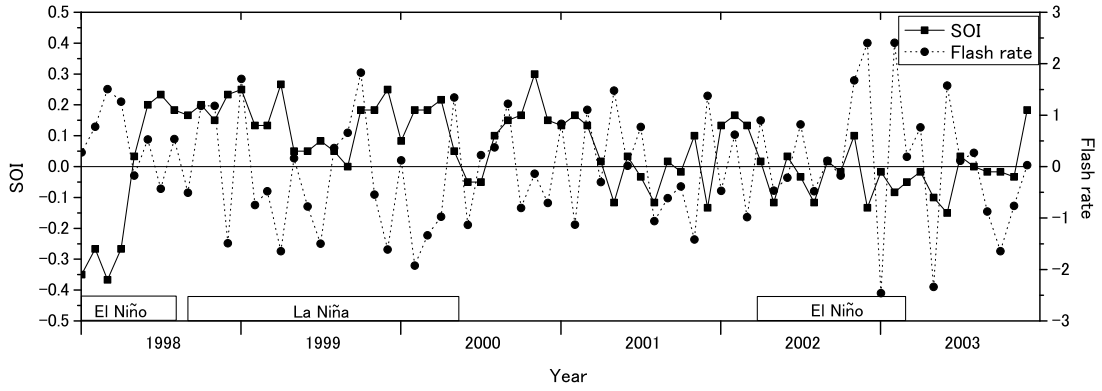

Figure 4.8: The monthly variation of SOI and the variation of the flash rate in EAR. In the period two El Niño and one La Niña are recorded.

May 2000 the index is -0.73. This analysis period includes the 1997-1998 El Niño period which is well-known as one of the strongest El Niño events in the last century [96]. This fact indicates that stronger El Niño causes stronger inverse correlation. The flash rate variability has a strong inverse correlation with SOI during El Niño and La Niña events. This means the lightning activity in EAR has strong dependence on the phase of the ENSO.

In order to find out what causes the contrast of the lightning activity, we focus on the areal distributions between El Niño and La Niña for several parameters. Figure 4.9 and 4.10 show the areal distributions of the anomaly of the flash rate and the rain count, respectively. The anomaly is derived as described below. First, the annual averages for all six years and only for El Niño or La Niña periods are created from the monthly data about the flash rate and the rain count. Then, the El Niño and La Niña annual averages are compared with their six-year averages about each parameter. For the flash rate anomaly, we do not show the flash rate less than 5 flashes per year in each 1° grid. From Figures 4.9, we can see the flash rate during the El Niño period is much higher than that during the La Niña period in a large region including East Asia, Indonesia, and Western Australia. These results are consistent with Figure 4.8 and the report of *Hamid et al.* [61]. The yellow ellipses in Figures 4.9 and 4.10 show the areas with the high flash rate anomaly. The rain count has clear difference with the boundary shown as the pink line in Figure 4.10. The rain count during the El Niño period is smaller than that during the La Niña period in the Western Pacific and Australia. These results agree with previous findings (e.g., [97]). From Figures 4.9 and 4.10, it is noticeable that the regions where the flash rate and the rain count increase are not the same. The flash rate increases despite the lower rain count in Western Australia and Indonesia during the El Niño period. In the La Niña period, the areal coverage of lower flash rate and higher rain count is larger than that of

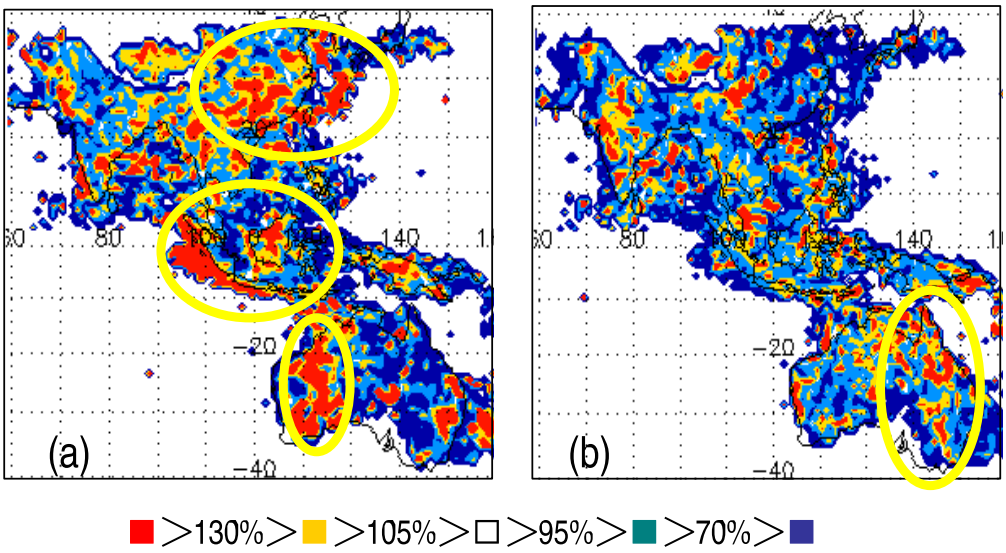

Figure 4.9: Distributions of the anomaly of the flash rate for the six-year average sampled on a 1°grid (a) El Niño and (b) La Niña.

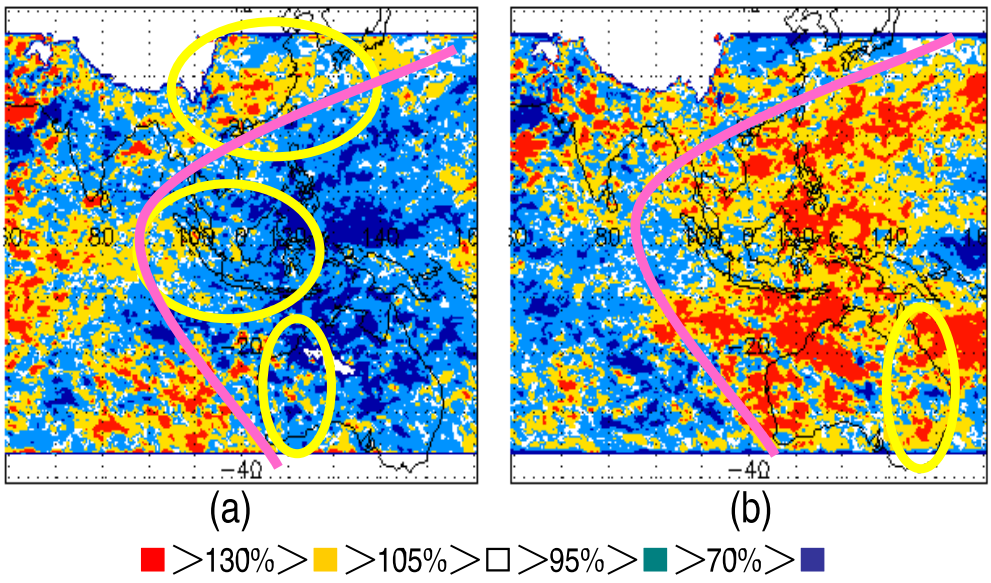

Figure 4.10: Distributions of the anomaly of the rain count for the six-year average sampled on a 0.5° grid, (a) El Niño and (b) La Niña. The pink line in this figure shows the boundary between increase and decrease in rain count.

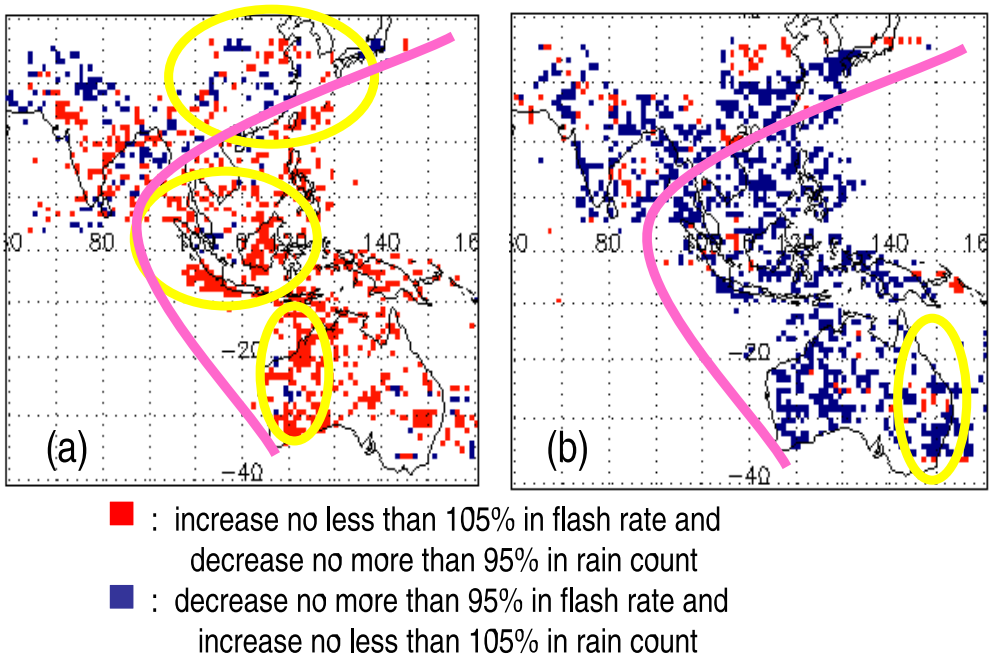

Figure 4.11: Distributions of the correlation between flash rate and rain count for the six-year average sampled on a 1° grid, (a) El Niño and (b) La Niña.

the six-year average.

To clarify this point, we plot the regions where the flash rate increases and the rain count decreases and, where the flash rate decreases and the rain count increases (see Figure 4.11). This figure shows a clear contrast between El Niño and La Niña. During the El Niño period the flash rate increases with less rain count and this tendency is especially enhanced in Western Australia and Indonesia. On the other hand during the La Niña period the flash rate decreases in spite of high rain count. These results indicate a distinct difference of convective activity between El Niño and La Niña periods.

The areal distributions of the anomaly of the variation of the radar reflectivity are shown in Figure 4.12. The method of calculating the anomaly is the same as in Figure 4.9. During the El Niño period on the west side of the pink line, the areal coverage of the higher radar reflectivity is larger than that of the six-year average while the La Niña shares the same characteristic on the east side of the pink line. In spite of the trend of the El Niño period, however, the Figure shows increase in radar reflectivity in Western Australia and Indonesia. Since high radar reflectivity is positively correlated with the accumulation of ice-phase condensate in the mixed phase region, the high radar reflectivity is positively correlated with strong updraft [79]. A larger accumulation of ice-phase and stronger updraft cause a more vigorous charge separation by collisions between graupel and ice particles [77, 78]. Therefore the higher flash rate in Western Australia and Indonesia is caused by these vigorous charge separations. Strong convective clouds in these areas

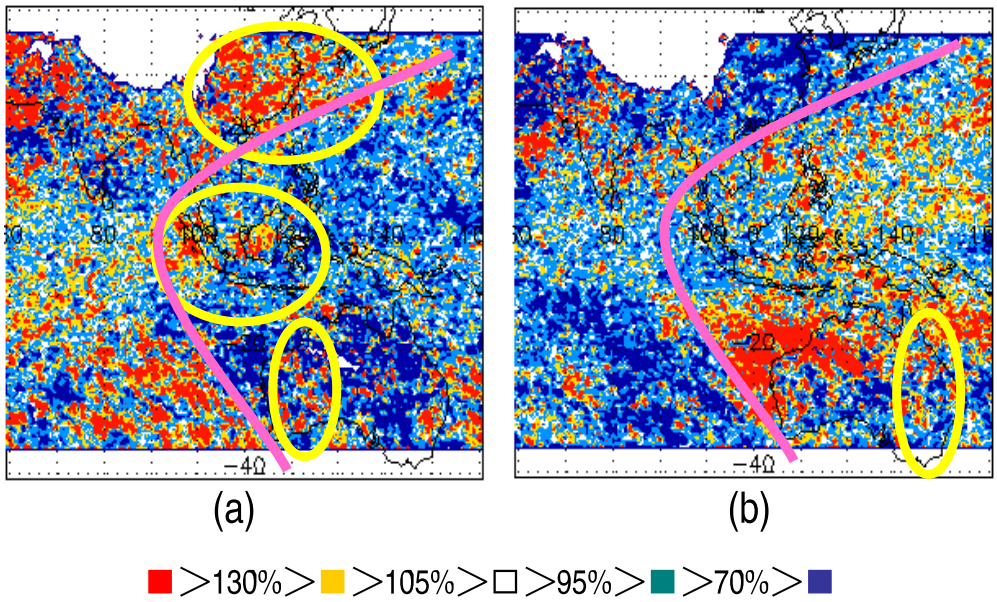

Figure 4.12: Distribution of variation of the radar reflectivity for convective clouds at an altitude of 6 km for the six-year average sampled on a 0.5° grid, (a) El Niño and (b) La Niña.

cause a high flash rate despite a low rain count.

Figure 4.13 represents the areal distributions of anomalies of the sea level pressure and the wind vector from the NCEP/NCAR Reanalysis Project. The method of calculating the anomaly is the same as before. Figure 4.13 shows that during El Niño period the sea level pressure in the WPR is much higher than that during the La Niña period. Furthermore the pressure over the ocean is higher than over the land during the El Niño period. From Figures 4.10 and 4.13, it is obvious that the rainfall frequency decreases in the region with the high sea level pressure. From Figure 4.13, we can find that the wind anomaly vector spreads from the region where the sea level pressure is high to the low pressure region over the land. Moreover the flash rate increases in the regions where wind anomaly vectors reach land from ocean, which are marked with arrows in Figure 4.13 (c) and (d).

4.3.4 Discussions

In this study, first we investigated the relationships between the ENSO events and lightning activity in the EAR using the data sets from LIS observations. There was an inverse correlation between lightning activities over the EAR and SOI. The strong ENSO events highly influence the lightning activity there. In other words, the lightning activity increases during the El Niño periods, and decreases during the La Niña period in this region. In addition we discussed the convective activities in the WPR during El Niño

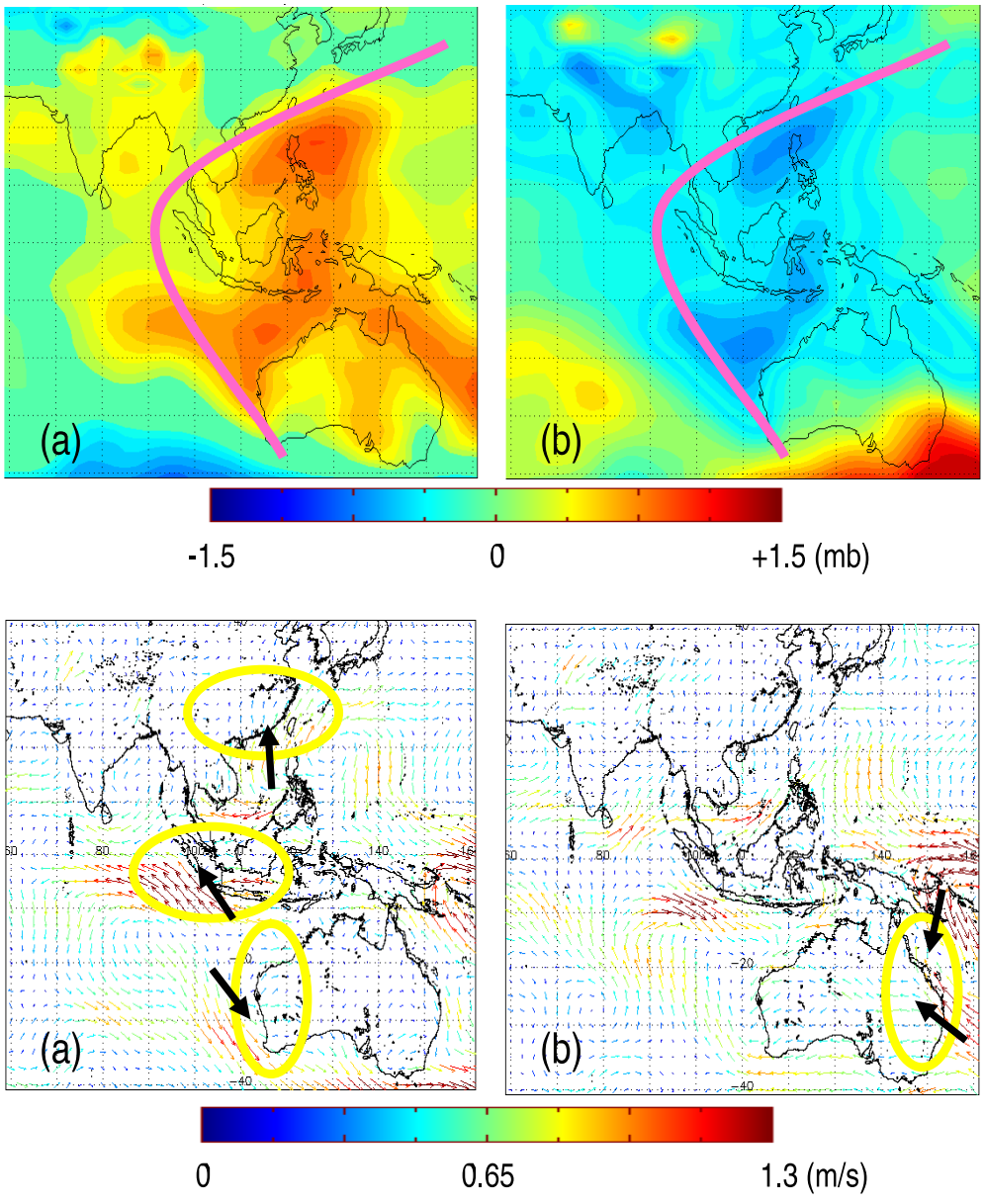

Figure 4.13: Distributions of the variation of the sea level pressure and wind vector for the six-year average, (a),(c) El Niño and (b), (d) La Niña.

and La Niña events using data sets obtained from LIS, PR and NCEP/NCAR Reanalysis Project. During El Niño period, the sea level pressure is higher than that of the six-year average, especially over the ocean including the north-east of Indonesia and north-west of Australia. These high-pressure systems decrease updrafts, and the rainfall frequencies are diminished in the same region. In the regions where the sea level pressure anomalies are higher over the ocean than over land, however, the wind vectors from the ocean to the land are remarkable. The moist air from the ocean is warmed over the land, and then makes strong updrafts. As a result, strong convective activity develops and makes much lightning activity over land. During the La Niña period, on the other hand, lower sea level pressures make several low-pressure systems and they increase rainfall frequency. Furthermore the contrast of the sea level pressure, which is low over the ocean and high over the land, causes the increase of wind from the land to the ocean. It is followed by the repression of strong updrafts and less deep convective activity. Though the results in this study are preliminary and further investigation and more evidence is needed, we found the implications of the change in convective activity due to El Niño and La Niña events on the lightning activity and their possible correlation with some parameters for storms.

4.4 Summary of the analyses of the TRMM data

In this chapter we conducted the data analyses using the LIS and PR data on the TRMM. The statistical analysis results shown in Section 4.2 and 4.3 were based on very long-term analysis, that is, eight years for Section 4.2 and six years for Section 4.3, respectively, so that these results possess high reliability. In Section 4.2, the parameterization of the thunderstorm was performed in terms of TRMM/PR and LIS observations. Though both north and south 35 degrees were the limit of observations due to the inclination of the TRMM orbit, the obtained results were meaningful from the aspect of statistics. The NFSC was shown to be proportional to the fifth power of the snow depth independent of regions and seasons. Moreover, the simple dimensional analyses agree with the results. A new universal fifth power law between lightning and convective clouds is established. In Section 4.3, the impacts on the lightning activity in the Western Pacific Ocean of the ENSO events were shown. We discussed the reason why lightning activity in the region was affected from the ENSO events. This study has given one key to solve the mechanisms of the ENSO events. The studies in the chapter have contributed to the atmospheric electricity to understand the charge separation mechanism in the thunderclouds.

Chapter 5

Conclusions

This thesis is devoted to study on radiations in association with lightning discharges. We conducted lightning observation campaign for energetic (Chapter 2) and electromagnetic radiations (Chapter 3), and performed observation data analyses for optical emissions from lightning (Chapter 4) in order to acquire knowledge about the physics of the atmospheric electricity, needless to say, lightning discharges. The summary of each chapter is shown.

The objective in Chapter 2 is to study the energetic radiation associated with lightning discharges. A field campaign was conducted during the Japanese winter thunderstorm season to observe radiation bursts associated with lightning discharges using a NaI scintillator and a thin plastic scintillator (PS), which primarily detects high energy electrons. We successfully recorded the bursts of high energy electrons with energies in excess of 100 keV from lightning discharges. It seems that these high energy electrons were produced by high energy photon interactions near the PS. Our observations suggest that not only negative leaders but also positive leaders can cause an increase in the NaI count rate.

The objective in Chapter 3 is to study the charge transfer mechanism of upward lightning and the microwave radiation associated with lightning. During winter thunderstorm season in Japan, a lightning observation campaign was conducted with the use of a microwave receiver, a VHF broadband digital interferometer (DITF), a capacitive antenna, and Rogowski coils. All the detection systems recorded one upward negative lightning stroke hitting a lightning protection tower. The upward lightning consists of only the Initial Stage (IS) with one upward positive leader and six initial continuing current (ICC) pulses. The six ICC pulses are sub-classified clearly into two types according to current pulse shapes. The type 1 ICC pulses have a higher geometric mean (GM) current peak of 17 kA and a shorter GM 10-90 % risetime of 8.9 μs, while the type 2 ICC pulses have a lower GM current peak of 0.34 kA and longer GM 10-90% risetime of 55 μs. The type 1 ICC pulses have the preceding negative leaders connecting to the channel of the continuing current. These negative leaders probably caused the current increases of the ICC pulses, which means that the negative leaders created the channels for the ICC pulses. The height of the space charge transferred by the ICC pulse was estimated about 700 m above sea level at most. We also recorded apparent increases in the microwave power

associated with the upward lightning. The microwave radiation sources seems to be the tip of the negative leaders and the lightning current.

The objective in Chapter 4 is to conduct statistical analyses and to study the mechanisms of the electrification in the thundercloud and the climate changes. The Lightning Imaging Sensor (LIS) and the Precipitation Radar (PR) aboard the Tropical Rainfall Measuring Mission (TRMM) were employed. We have two main results (Section 4.2 and Section 4.3) in this study.

In Section 4.2, coincident data from the PR and the LIS aboard the TRMM are used to examine the correlation between the Number of lightning Flash per Second per Convective cloud (NFSC) and the snow depth. The snow depth is defined as the height from the freezing level to the echo top height. It is found that the NFSC is proportional to the fifth power of the snow depth. Additionally, it should be noticed that the relationship does not have regional and seasonal dependencies. In other words, the NFSC is constantly proportional to the fifth power of the snow depth. Two simple dimensional analyses indicate that the fifth power of the snow depth is proportional to the stored static electric energy and to the temporal differentiation of the electric charge generated in the convective cloud. These analyses agree with the outcomes from the TRMM observations. In conclusion, a new universal fifth power law between lightning activity and convective clouds is established.

In Section 4.3, the remarkable contrasts between El Niño and La Niña in the East/ Southern-East Asia region and the Western Pacific Region are reported. One is that the lightning flash rate in the East/South-East Asia region shows a clear inverse correlation with the Southern Oscillation Index (SOI). The lightning activity increases during the El Niño period and decreases during the La Niña period in this area. The other is that the contrast of the areal distribution of the variation of the flash rate in the Western Pacific region. During the El Niño period the moist air from the ocean is warmed over the land, and that makes strong updrafts in high-pressure systems over the oceanic area. As a result, well-developed cumulonimbus with frequent lightning activity is observed in the coastal area. During the La Niña period, low-pressure systems on the land cause the increase of rainfall frequency with less lightning activity.

These studies in Chapter 4 have contributed to the atmospheric electricity to understand the mechanisms of the electrification in the thunderclouds and the climate change.

Bibliography

[1] Rakov, V. A. and M. A. Uman (2003), Introduction, in Lightning: Physics and Effects, chap.1, 1–23, *Cambridge Univ. Press, Cambridge, U. K.*

[2] Rakov, V. A. and M. A. Uman (2003), Downward negative lightning discharges to ground, in Lightning: Physics and Effects, chap.4, 108–213, *Cambridge Univ. Press, Cambridge, U. K.*

[3] Rakov, V. A. and M. A. Uman (2003), Upward lightning initiated by ground-based objects, in Lightning: Physics and Effects, chap.6, 241–264, *Cambridge Univ. Press, Cambridge, U. K.*

[4] Rakov, V. A. and M. A. Uman (2003), Cloud discharges, in Lightning: Physics and Effects, chap.9, 321–345, *Cambridge Univ. Press, Cambridge, U. K.*

[5] Berger, K., R. B. Anderson, and H. Kroninger (1975), Parameters of lightning flashes, *Electra*, *80*, 223–237.

[6] Lay, E. H., A. R. Jacobson, R. H. Holzworth, C. J. Rodger, and R. L. Dowden (2004), Local time variation in land/ocean lightning flash density as measured by the World Wide Lightning Location Network, *J. Geophys. Res.*, *112*, D13111, doi:10.1029/2006JD007944.

[7] Bent, R. B. and W. A. Lyons (1984), Theoretical evaluations and initial operational experiences of LPATS (Lightning Position and Tracking System) to monitor lightning ground strikes using a time-of-arrival (TOA) technique, paper presented at the 7th International Conference on Atmospheric Electricity, Int. Comm. on Atmos. Electr., N. Y., 3–8 June.

[8] Mardiana, R., and Z. Kawasaki (2000), Broadband radio interferometers utilizing sequential triggering technique for locating fast-moving electromagnetic sources emitted from lightning, *IEEE Trans. Instrum. Meas.*, *49*, 376–381.

[9] Morimoto, T., A. Hirata, Z. Kawasaki, T. Ushio, A. Matsumoto, and J. H. Lee (2004), An operational VHF broadband digital interferometer for lightning monitoring, *IEEJ Trans. Fundam. Mater.*, *124*(12), 1232–1238.

[10] Morimoto, T., Z.-I. Kawasaki, and T. Ushio (2005), Lightning observations and consideration of positive charge distribution inside thunderclouds using VHF broadband interferometry, *Atmos. Res., 76*, 445–454.

[11] Rakov, V. A., et al. (1998), New insights into lightning processes gained from triggered-lightning experiments in Florida and Alabama, *J. Geophys. Res.*, *103*(D12), 14,117–14,130.

[12] Christian, H., et al. (1999), The Lightning Imaging Sensor, paper presented at the 11th International Conference on Atmospheric Electricity, Int. Comm. on Atmos. Electr., Guntersville, Ala., 7–11 June.

[13] Wang, D., N. Takagi, T. Watanabe, V. A. Rakov, and M. A. Uman (1999), Observed leader and return-stroke propagation characteristics in the bottom 400 m of a rocket-triggered lightning channel, *J. Geophys. Res.*, *102*(D12), 14,369–14,376.

[14] Fisher, R. J., G. H. Schnetzer, R. Thottappillil, V. A. Rakov, M. A. Uman, and J. D. Goldberg (1993), Parameters of triggered-lightning flashes in Florida and Alabama, *J. Geophys. Res.*, *98*(D12), 22,887–22,902.

[15] Torii, T., M. Takeishi, and T. Hosono (2002), Observation of gamma-ray dose increase associated with winter thunderstorm and lightning activity, *J. Geophys. Res.*, *107*(D17), 4324, doi:10.1029/2001JD000938.

[16] Tsuchiya, H., et al. (2007), Detection of high-energy gamma rays from winter thunderclouds, *Phys. Rev. Lett.*, *99*(16), id.165002.

[17] Gurevich, A. V., and K. P. Zybin (2005), Runaway breakdown and the mysteries of lightning, *Phys. Today*, *58*, 37–43.

[18] Dwyer, J. R. et al. (2003), Energetic radiation produced during rocket-triggered lightning, *Science*, *299*, 694–697.

[19] Dwyer, J. R., et al. (2004), Measurements of x-ray emission from rocket-triggered lightning, *Geophys. Res. Lett.*, *31*, L05118, doi:10.1029/2003GL018770.

[20] Dwyer, J. R., et al. (2004), A ground level gamma-ray burst observed in association with rocket-triggered lightning, *Geophys. Res. Lett.*, *31*, L05119, doi:10.1029/2003GL018771.

[21] Dwyer, J. R., et al. (2005), X-ray bursts associated with leader steps in cloud-to-ground lightning, *Geophys. Res. Lett.*, *32*, L01803, doi:10.1029/2004GL021782.

[22] Williams, E. R., et al. (2006), Lightning flashes conducive to the production and escape of gamma radiation to space, *J. Geophys. Res.*, *111*, D16209, doi:10.1029/2005JD006447.

[23] Williams, E., R. (2006), Problems in lightning physics - The role of polarity asymmetry, *Plasma Sources Sci. Technol.*, *15*, S91–S108.

[24] Gurevich, A. V., G. M. Milikh, and R. Roussel-Dupre (1992), Runaway electron mechanism for air breakdown and preconditioning during a thunderstorm, *Phys. Lett. A*, *165*, 463–468.

[25] Torii, T., T. Nishijima, Z. Kawasaki, and T. Sugita (2004), Downward emission of runaway electrons and bremsstrahlung photons in thunderstorm electric fields, *Geophys. Res. Lett.*, *31*, L05113, doi:10.1029/2003GL019067.

[26] J. R. Dwyer (2005), The initiation of lightning by runaway air breakdown, *Geophys. Res. Lett.*, *32*, L20808, doi:10.1029/2005GL023975.

[27] Kitagawa, N. and K. Michimoto (1994), Meteorological and electrical aspects of winter thunderclouds, *J. Geophys. Res.*, *99*(D5), 10,713–10,721.

[28] Berger, K. (1967), Novel observation on lightning discharges: Results of research on Mount San Salvatore, *J. Franklin Inst.*, *283*, 478–525.

[29] Wang, D., N.Takagi, T.Watanebe, H. Sakurano, and M. Hashimoto (2008), Observed characteristics of upward leaders that are initiated from a windmill and its lightning protection tower, *Geophys. Res. Lett.*, *35*, L02803, doi:10.1029/2007GL032136.

[30] Wilson, C. T. R. (1925), The electric field of the thundercloud and some of its effects, *Proc. Phys. Soc. London, Sect. D*, *37*, 32–37.

[31] Moore, C. B., K. B. Eack, G. D. Aulich, and W. Rison (2001), Energetic radiation associated with lightning stepped-leaders, *Geophys. Res. Lett.*, *28*, 2141–2144.

[32] Fishman, G. J., et al. (1994), Discovery of intense gamma-ray flashes of atmospheric origin, *Science*, *264*, 1313–1316.

[33] Smith, D. M., L. I. Lopez, R. P. Lin, and C. P. Barrington-Leigh (2005), Terrestrial gamma-ray flashes observed up to 20 MeV, *Science*, *307*,1085–1088.

[34] Kawasaki, Z., S. Yoshihashi, and Lee Jong Ho (2002), Verification of bi-directional leader concept by interferometer observations, *J. Atmos. Electr.*, *22*(2), 55–79.

[35] Kawasaki, Z.-I. and Mazur V. (1992), Common physical processes in natural and triggered lightning in winter storms in Japan, *J. Geophys. Res.*, *97*, 12,935–12,945.

[36] Rakov, V. A., M. A. Uman, G. R. Hoffman, M. W. Masters, and M. Brook (1996), Bursts of pulses in lightning electromagnetic radiation: Observations and implications for lightning test standard, *IEEE Trans. Electromagn. Compat.*, *38*, 156–164.

[37] Dwyer, J. R., H. K. Rassoul, Z. Saleh, M. A. Uman, J. Jerauld, and J. A. Plumer (2005), X-ray bursts produced by laboratory sparks in air, *Geophys. Res. Lett.*, *32*, L20809, doi:10.1029/2005GL024027.

[38] Wang, D., N. Takagi, and T. Watanabe (2007), Observed characteristics of luminous variation events during the initial stage of upward positive leaders, *J. Atmos. Electr.*, *27*(1), 61–68.

[39] McEachron, K. B. (1939), Lightning to the Empire State Building, *J. Franklin Inst.*, *227*, 149–217.

[40] Berger, K. and E. Vogelsanger (1966), Photographische Blizuntersuchungen der Jahre 1955-1965 auf dem Monte San Salvatore, *Bull. Schweiz. Elektrotech. Ver. 57*, 599–620.

[41] Fuchs, F., E. U. Landers, R. Schmid, and J. Wiesinger (1998), Lightning current and magnetic field parameters caused by lightning strokes to tall structures relationg to interference of electronic system, *IEEE Trans. Electromagn. Compat. 40*, 444–451.

[42] Rakov, V. A., D. E. Crawford, K. J. Rambo, G. H. Schnetzer, M. A. Uman, and R. Thottappillil (2001), M-component mode of charge transfer to ground in lightning discharges, *J. Geophys. Res.*, *106*(D19), 22,817–22,831.

[43] Rakov, V. A., R. Thottappillil, M. A. Uman, and P. P. Barker (1995), Mechanism of the lightning M component, *J. Geophys. Res.*, *100*(D12), 25,701–25,710.

[44] Wang, D., V. A. Rakov, M. A. Uman, M. I. Fernandez, K. J. Rambo, G. H. Schnetzer, and R. J. Fisher (1999), Characterization of the initial stage of negative rocket-triggered lightning, *J. Geophys. Res.*, *104*(D4), 4213–4222.

[45] Thottappillil, R., J. D. Goldberg, V. A. Rakov, and M. A. Uman (1995), Properties of M components from currents measured at triggered lightning channel base, *J. Geophys. Res.*, *100*, 25,711–25,720.

[46] Miki, M., et al. (2005), Initial stage in lightning initiated from tall objects and in rocket-triggered lightning, *J. Geophys. Res.*, *110*, D02109, doi:10.1029/2003JD004474.

[47] Gorin, B. N., G. S. Sakharova, V. V. Tikhomirov, and A. V. Shkilev (1975), Results of studies of lightning strikes to the Ostankino TV tower, *Trudy ENIN*, *43*, 63–77.

[48] Miki, M., et al. (2006), Characterization of current pulses superimposed on the continuous current in upward lightning initiated from tall objects and in rocket-triggered lightning, paper presented at the 28th International Conference on Lightning Protection, Kanazawa, Japan, 18–22 September.

[49] Oetzel, G. N. and E. T. Pierce (1969), The radio emissions from close lightning, in Planetary Electrodynamics, *1*, 543–571, *Gordon and Breach, New York, USA.*

[50] Rust, W. D., P. R. Krehbiel, and A. Shalanta (1979), Measurements of radiation from lightning at 2200 MHz, *Geophys. Res. Lett.*, *6*(2), 85–88.

[51] Kitterman, C. G. (1981), Concurrent lightning flashes on two television transmission towers, *J. Geophys. Res.*, *86*(C6), 5378–5380.

[52] Miyake, K., T. Suzuki, M. Takashima, M. Takuma, and T. Tada (1990), Winter lightning on Japan Sea coast - Lightning striking frequency to tall structures, *IEEE Trans. Pow. Del. 5*, 1370–1376.

[53] Yoshida, S., et al. (2008), High energy photon and electron bursts associated with upward lightning strokes, *Geophys. Res. Lett.*, *35*, L10804, doi:10.1029/2007GL032438.

[54] Rakov, V. A. (1999), Lightning discharges triggered using rocket-and-wire techniques, *Recent Res. Dev. Geophys.*, *2*, 141–171.

[55] Kitagawa, N. (1992), Charge distribution of winter thunderclouds, *Res. Lett. Atmos. Electr.*, *12*, 143–153.

[56] Suzuki, T. (1992), Long term observation of winter lightning on Japan Sea coast, *Res. Lett. Atmos. Electr*. *12*, 54–56.

[57] Ishii, M. and Shindo T. (1995), Recent topics on research of lightning and lightning protection in Japan, *Elektrotechnik und Informationstechnik*, *112*(6), 262–272.

[58] Japan Aerospace Exploration Agency (JAXA) HP: http://www.eorc.jaxa.jp/.

[59] Simpson, J., R. F. Adler, and G. R. North (1988), A proposed Tropical Rainfall Measuring Mission (TRMM) satellite, *Bull. Am. Meteorol. Soc.*, *69*, 278–295.

[60] Williams E. R. (1992), The Schumann Resonance: A global tropical thermometer, *Science*, *256*, 1184–1187.

[61] Hamid E. Y., Z.-I. Kawasaki, and R. Mardiana (2001), Impact of the 1997-98 El Niño event on lightning activity over Indonesia, *Geophys. Res. Lett.*, *28*(1), 147–150.

[62] Goodman, S. J., D. E. Buechler, K. Knupp, K. Driscoll, and E. W. McCaul Jr. (2000), The 1997–98 El Niño event and related wintertime lightning variations in the Southeastern United States, *Geophys. Res. Lett.*, *27*(4), 541–544.

[63] Yoshida S., T. Morimoto, T. Ushio, and Z. Kawasaki (2007), ENSO and convective activities in Southeast Asia and western Pacific, *Geophys. Res. Lett.*, *34*, L21806, doi:10.1029/2007GL030758.

[64] Levy, H., W. J. Moxim, and P. S. Kasibhatla (1996), A global three-dimensional time-dependent lightning source of tropospheric NO_x, *J. Geophys. Res.*, *101*(D17), 22,911–22,922.

[65] Franzblau, E. and C. J. Popp (1989), Nitrogen oxides produced from lightning, *J. Geophys. Res.*, *94*(D8), 11,089–11,104.

[66] Williams, E. R. (1985), Large-scale charge separation in thunderclouds, *J. Geophys. Res.*, *90*(D4), 6013–6025.

[67] Price, C. and D. Rind (1992), A simple lightning parameterization for calculating global lightning distributions, *J. Geophys. Res.*, *97*(D9), 9919–9933.

[68] Michalon, B. N., A. Nassif, T. Saouri, J. F. Royer, and C. A. Pontikis (1999), Contribution to the climatological study of lightning, *Geophys. Res. Lett.*, *26*(20), 3097–3100.

[69] Ushio T., S. J. Heckman, D. J. Boccippio, H. J. Christian, and Z.-I. Kawasaki (2001), A survey of thunderstorm flash rates compared to cloud top height using TRMM satellite data, *J. Geophys. Res.*, *106*(D20), 24,089–24,095.

[70] Petersen, W. A., H. J. Christian, and S. A. Rutledge (2005), TRMM observations of the global relationship between ice water content and lightning, *Geophys. Res. Lett.*, *32*, L14819, doi:10.1029/2005GL023236.

[71] Vonnegut, B. (1963), Some facts and speculations concerning the origin and role of thunderstorm electricity, *Meteorol. Monogr.*, *5*, 224–241.

[72] Jacobson, E. A., and E. P. Krider (1976), Electrostatic field changes produced by Florida lightning, *J. Atmos. Sci.*, *33*, 103–117.

[73] Livingston, J. M., and E. P. Krider (1978), Electric fields produced by Florida thunderstorms, *J. Geophys. Res.*, *83*, 385–401.

[74] Shackford, C. R. (1960), Radar indications of a precipitation-lightning relationship in New England thnderstorms, *J. Meteor.*, *17*, 15–19.

[75] Price, C., J. Penner, and M. Prather (1997), NO_x from lightning, 1, Global distribution based on lightning physics, *J. Geophys. Res.*, *102*, 5929–5941.

[76] Boccippio, D. J. (2001), Lightning scaling relations revisited, *J. Atmos. Sci.*, *59*, 1086–1104.

[77] Takahashi, T. (1978), Riming electrification as a charge generation mechanism in thunderstorms, *J. Atmos. Sci.*, *35*, 1536–1548.

[78] Takahashi, T., T. Tajiri, and Y. Sonoi (1999), Charges on graupel and snow crystals and the electrical structure of winter thunderstorms, *J. Atmos. Sci.*, *56*, 1561–1578.

[79] May, P. T., A. R. Jameson, T. D. Keenan, P. E. Johnston, and C. Lucas (2002), Combined wind profiler/polarimetric radar studies of the vertical motion and microphysical characteristics of tropical sea breeze thunderstorms, *Mon. Wea. Rev.*, *130*, 2228–2239.

[80] Peckham, D. W., M. A. Uman, and C. E. Wilcox Jr. (1984), Lightning phenomenology in the Tampa Bay area, *J. Geophys. Res.*, *89*(D7), 11,789–11,805.

[81] Wang, K.-Y. and S.-A. Liao (2006), Lightning, radar reflectivity, infrared brightness temperature, and surface rainfall during the 2–4 July 2004 severe convective system over Taiwan area, *J. Geophys. Res.*, *111*, D05206, doi:10.1029/2005JD006411.

[82] Thomas, R. J., P. R. Krehbiel, W. Rison, T. Hamlin, D. J. Boccippio, S. J. Goodman, and H. J. Christian (2000), Comparison of ground-based 3-dimensional lightning mapping observations with satellite-based LIS observations in Oklahoma, *Geophys. Res. Lett.*, *27*(12), 1703–1706.

[83] Ushio, T., S. Hechman, K. Driscoll, D. Boccippio, H. Christian, and Z.-I. Kawasaki (2002), Cross-sensor comparison of the Lightning Imaging Sensor (LIS), *Int. J. Remote Sensing*, *23*(13), 2703–2712.

[84] Rutledge, S. A., E. R. Williams, and T. D. Keenan (1992), The down under Doppler and electricity experiment (DUNDEE): Overview and preliminary results, *Bull. Am. Meteorol. Soc.*, *73*, 3–16.

[85] Takahashi T. (1990), Near absence of lightning in torrential rainfall producing Micronesian thunderstorms, *Geophys. Res. Lett.*, *17*(13), 2381–2384.

[86] Christian, H. J., et al. (2003), Global frequency and distribution of lightning as observed from space by the Optical Transient Detector, *J. Geophys. Res.*, *108*(D1), 4005, doi:10.1029/2002JD002347.

[87] Stolzenburg M., T. C. Marshall, W. D. Rust, and D. L. Bartels (2002), Two simultaneous charge structures in thunderstorm convection, *J. Geophys. Res.*, *107*(D18), 4352, doi:10.1029/2001JD000904.

[88] Baker, M. B., A. M. Blyth, H. J. Christian, J. Latham, K. L. Miller, and A. M. Gadian (1999), Relationships between lightning activity and various thundercloud parameters: satellite and modelling studies, *J. Atmos. Res.*, *51*, 221–236.

[89] Blyth, A. M., H. J. Christian, K. Driscoll, A. M. Gadian, and J. Latham (2001), Determination of ice precipitation rates and thunderstorm anvil ice contents from satellite observations of lightning, *Atmos. Res.*, *59–60*, 217–229.

[90] Deierling, W., J. Latham, W. A. Petersen, S. M. Ellis, and H. J. Christian Jr. (2005), On the relationship of thunderstorm ice hydrometeor characteristics and total lightning measurements, *J. Atmos. Res.*, *76*, 114–126.

[91] Williams, E. R. (1988), The electrification of thunderstorms, *Sci. Amer.*, *269*, 88–99.

[92] Locatelli, J. D. and P. V. Hobbs (1974), Fall speeds and masses of solid precipitation particles, *J. Geophys. Res.*, *79*, 2185–2197.

[93] Rasmusson E. M., and T. H. Carpenter (1983), The relationship between eastern equatorial Pacific sea surface temperatures and rainfall over India and Sri Lanka. *Mon. Wea. Rev.*, *111*, 517–528.

[94] Williams E. R. (2005), Lightning and climate: A review, *J. Atmos. Res.*, *76*, 272–287.

[95] Ropelewski, C. F., and P. D. Jones (1987), An extension of the Tahiti-Darwin Southern Oscillation Index, *Mon. Wea. Rev.*, *115*, 2161–2165.

[96] Chandra, S., J. R. Ziemke, W. Min, and W. G. Read (1998), Effects of 1997-1998 EL Niño on tropospheric ozone and water vapor, *Geophys. Res. Lett.*, *25*(20), 3867–3870.

[97] Curtis S. and R. F. Adler (2003), Evolution of El Niño-precipitation relationships from satellites and gauges, *J. Geophys. Res.*, *108*(D4), 4153, doi:10.1029/2002JD002690.

List of Publications

Journal Papers

A.1 Morimoto, T., S. Yoshida, Y. Sato, Z.-I. Kawasaki, and T. Ushio (2003) Parameterization of the lightning flash rate using TRMM (PR/LIS) data (in Japanese), *T*enki, *50*, 11, 5-14.

A.2 Yoshida, S., T. Morimoto, T. Ushio, and Z.-I. Kawasaki (2007), ENSO and convective activities in South-East Asia and Western Pacific, *Geophys. Res. Lett.*, *34*, L21806, doi:10.1029/2007GL030758, 2007.

A.3 Yoshida, S., T. Morimoto, T. Ushio, and Z.-I. Kawasaki (2008), Energetic Radiation Bursts associated with lightning, *IEEJ Transactions on Fundamentals and Materials*, *128*, 1, 9-13.

A.4 Yoshida, S., T. Morimoto, T. Ushio, Z.-I. Kawasaki, T. Torii, D. Wang, N. Takagi, and T. Watanabe (2008), High energy photon and electron bursts associated with upward lightning strokes, *Geophys. Res. Lett.*, *35*, L10804, doi:10.1029/2007GL032438.

Proceedings of International Conferences

B.1 Kawasaki, Z.-I., T. Ushio, S. Yoshida, and Y. Sato, What we have learned by TRMM/PR and LIS, 12th International Conference on Atmospheric Electricity, Versailles France, June 2003.

B.2 Kawasaki, Z.-I., S. Yoshida, and T. Morimoto National wide SAFIR network in Japan, 12th International Conference on Atmospheric Electricity, Versailles France, June 2003.

B.3 Yoshida, S., M. Sato, T. Morimoto, T. Ushio, Z.-I. Kawasaki, and T. Torii, Radiation Bursts Synchronizing with Lightning Discharges in Hokuriku, Japan, 13th International Conference on Atmospheric Electricity, Beijing China, August 2007.

B.4 Yoshida, S., T. Morimoto, N. Nakazato, T. Ushio, Z.-I. Kawasaki Global impact of ENSO events by TRMM observations, 13th International Conference on Atmospheric Electricity, Beijing China, August 2007.

B.5 Yoshida, S., T. Morimoto, T. Ushio, and Z.-I. Kawasaki, ENSO and convective activities in Southeast Asia and the western Pacific, The 3rd TRMM International Science Conference, Nevada, USA, February, 2008.